NTNU – Trondheim
Norwegian University of
Science and Technology

Texturing of lead-free piezoelectric ceramics

Gerhard Henning Olsen

Chemical Engineering and Biotechnology
Submission date: June 2012
Supervisor: Mari-Ann Einarsrud, IMTE
Co-supervisor: Astri Bjørnetun Haugen, IMTE
Tor Grande, IMTE

Norwegian University of Science and Technology
Department of Materials Science and Engineering

Declaration

I hereby declare that the work presented in this document has been performed independently and in accordance with the rules and regulations of the Norwegian University of Science and Technology (NTNU).

Trondheim, 29 June 2012

Gerhard Olsen

Preface

This thesis is submitted to the Norwegian University of Science and Technology (NTNU), as part of the requirements for the degree of Master of Science/Sivilingeniør. The work presented in this thesis has been carried out at the Department of Materials Science and Engineering at NTNU between 23 January and 29 June, 2012, where Professor Mari-Ann Einarsrud has supervised the work, and Ph.D. candidate Astri Bjørnetun Haugen and Professor Tor Grande have served as co-supervisors.

I would like to thank my supervisors for the effort they have laid down in guiding me through this work. My main supervisor Mari-Ann Einarsrud has provided me with constructive and helpful feedback throughout the entire last year, from the planning of the work in January, to the writing of this thesis in June. My co-supervisor Astri Bjørnetun Haugen has also been very helpful all the way, always taking time to help me with big and small issues in connection with my day-to-day work, and she also provided me with the KNN and $K_2Nb_4O_{11}$ powders I used. My second co-supervisor, Tor Grande, deserves credit for first convincing me about exploring the fascinating world of piezoelectric materials.

I would also like to acknowledge both the rest of my co-workers in the Ferroics group, and the various people associated with the Ceramics group in general. Special credit goes to Dr. Maxim Morozov for giving me an introduction to dielectric spectroscopy, which became a nice addition to my work during the last couple of weeks. Finally, I would like to thank all technical staff at the department, for giving me equipment training and help with various practical problems.

Abstract

A procedure for texturing of lead-free piezoelectric ceramics based on sodium potassium niobate (KNN) was investigated with respect to texturing procedure and choice of materials.

Material compositions that were considered include KNN with and without addition of 0.5 mol% MnO, and KNN modified with Li and Ta (KNNLT), and Mn substituted into the A or B site of the perovskite structure. The two compositions KNN-Mn and KNNLT-Mn(A) compositions were further investigated as candidate materials for texturing.

Textured samples of the two materials were made by tape casting and templated grain growth, using needle-shaped KNN particles as templates, while non-textured reference samples were made by conventional sintering of powders. Both textured and non-textured dense materials were characterized with respect to density, degree of texture and piezoelectric and dielectric properties. The non-textured materials sintered to high relative densities of 93.9 % for KNN-Mn and 96.7 % for KNNLT-Mn(A). A converse piezoelectric coefficient of over 250 pm V^{-1} was measured for non-textured KNNLT-Mn(A), and around 200 pm V^{-1} for KNN-Mn.

Texturing led to a lower relative density of both compositions, 89.1 % for KNN-Mn and 92.1 % for KNNLT-Mn(A). The piezoelectric performance of KNN-Mn was not significantly affected by the texturing procedure, while the piezoelectric performance of KNNLT-Mn(A) became significantly poorer. This is due to the formation of a secondary phase in KNNLT-Mn(A) during sintering, which is probably caused by the compositional mismatch between the templates and the fine-grained matrix powder.

Based on the results, and a theoretical consideration of the texturing procedure, a different choice of template particles is suggested for further work on texturing of KNN-based materials.

Sammendrag

En metode for teksturering av blyfrie piezoelektriske keramer basert på kaliumnatriumniobat (KNN) er blitt vurdert med hensyn på tekstureringsmetode og materialvalg.

Materialsammensetninger som er blitt vurdert, er KNN med og uten tilsetning av 0.5 mol% MnO, og Li- og Ta-modifisert KNN (KNNLT) med Mn substituert inn på A- eller B-plass i perovskittstrukturen. Sammensetningene KNN-Mn og KNNLT-Mn(A) ble undersøkt videre som kandidater for fremstilling av teksturerte materialer.

Teksturerte prøver av begge materialsammensetninger ble laget ved båndstøping og templatstyrt kornvekst, med nåleformede KNN-partikler som templater. Uteksturerte referanseprøver ble laget ved alminnelig sintring av pulver. Både teksturerte og uteksturerte prøver ble karakterisert med hensyn på tetthet, grad av tekstur og piezo- og dielektriske egenskaper. De uteksturerte materialene oppnådde høy relativ tetthet under sintring, 93,9 % for KNN-Mn og 96,7 % for KNNLT-Mn(A). En piezoelektrisk koeffisient på over 250 pm V^{-1} ble målt for uteksturert KNNLT-Mn(A), og omlag 200 pm V^{-1} for KNN-Mn.

Teksturering førte til lavere relativ tetthet i begge materialsammensetninger, med 89,1 % for KNN-Mn og 92,1 % for KNNLT-Mn(A). De piezoelektriske egenskapene til KNN-Mn ble ikke påvirket i nevneverdig grad av tekstureringen, mens de for KNNLT-Mn(A) ble betydelig dårligere. Dette skyldes dannelse av en sekundærfase i KNNLT-Mn(A) under sintringen, som sannsynligvis utløses av den sammensetningsmessige forskjellen mellom templatene og det finkornede pulveret.

Basert på de oppnådde resultatene, samt teoretiske betraktninger omkring tekstureringsmetoden, foreslås en annen type templatpartikler for videre arbeid med teksturering av KNN-baserte materialer.

Contents

Chapter 1

Introduction

1.1 Motivation

The piezoelectric effect has been known at least since 1880, when the Curie brothers, Jacques and Pierre, for the first time reported that certain crystals developed an electric polarization when a stress was applied to them. This effect was found in many naturally occurring single crystals, such as quartz, tourmaline and sugar. Over the years, both natural and man-made piezoelectrics have found their use in various applications, both in the form of single crystals and, more recently, ceramics. Piezoelectric ceramics are now used in devices as diverse as phonograph pickups, ultrasound imaging equipment, sonars, loudspeaker elements, inkjet printers, actuators for automatic focusing mechanisms in cameras and microscopes, and high-voltage generators for gas grill lighters, to name but a few.[1]

One of the most widely used piezoelectric ceramics is PZT, or lead zirconate titanate.[2] It has very good piezoelectric properties, but contains more than 60 % by weight of lead. A directive of the European Union issued in 2003[3] has laid bounds on the use of lead and other potentially harmful elements in electronics, but for lead-containing oxide ceramics such as PZT, an exception has been made due to there being no technologically realistic alternatives to their use. That is, PZT components are still allowed in the EU until suitable replacements can be found.

In the years following the issue of this EU directive, research into lead-free piezoelectric materials has bloomed.[4] One class of possible candidates for the replacement of lead-containing piezoceramics is the alkali niobates,

among them sodium potassium niobate, or KNN. A major breakthrough in this research happened in 2004, when a Japanese research group reported[5] that the piezoelectric performance of certain KNN-based materials could be enhanced through the technique of texturing, thereby obtaining properties comparable to commercial PZT-based materials. This has lead to an increased interest in KNN-based materials over the last years, but there are still several challenges that need to be addressed before these materials can be viewed as realistic candidates for the replacement of lead-containing piezoceramics.

1.2 Aim of this work

The aim of this Master's thesis is to prepare textured lead-free piezoelectric ceramics. The material system will be KNN modified with Mn (KNN-Mn) and with Li, Ta and Mn (KNNLT-Mn). The materials will be characterized with respect to sintering behaviour, microstructure and piezoelectric performance. The textured materials will be characterized with respect to degree of texture, and compared with non-textured reference materials. A theoretical consideration of crystallography and the fundamental justification for texturing will constitute a significant part of the work.

The thesis is a natural continuation of the author's specialization project "Texturing of lead-free piezoceramics",[6] and is related to previous studies of KNN materials by M.Sc. students Lars-Petter Bjørkeng[7] and Jon Martinsen Strand,[8] and of Ph.D. candidate Francesco Madaro,[9] who have all contributed to the lead-free materials research at NTNU.

Chapter 2

Background

2.1 Piezoelectricity

Phenomenological description

Piezoelectricity is the phenomenon where an electric polarization develops in a material as a response to applied mechanical strain. This is known as the *direct piezoelectric effect*. The reverse effect, also known as the *converse piezoelectric effect*, involves the material expanding or contracting when exposed to an electric field. This is illustrated in Figure 2.1.

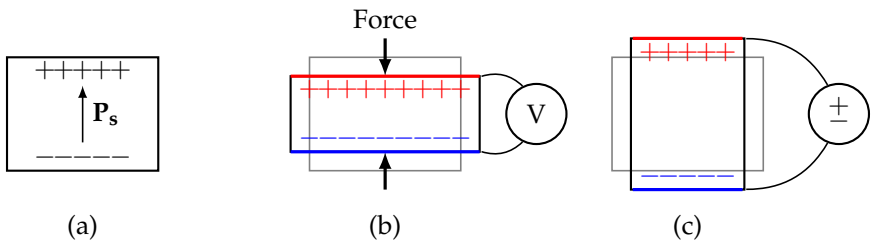

FIGURE 2.1: Illustration of the piezoelectric effect: (a) Material in original state with spontaneous polarization $\mathbf{P_s}$ indicated; (b) direct piezoelectric effect, where a surface charge develops as a response to applied mechanical strain; (c) converse piezoelectric effect, where the material expands when a voltage of the same sign as the spontaneous polarization is applied.

A basic description of the piezoelectric effects in mathematical terms is

$$P = d\sigma \text{ (direct effect)} \tag{2.1}$$

$$\epsilon = dE \text{ (converse effect)}, \tag{2.2}$$

where P is electric polarization, σ is mechanical stress, ϵ is strain and E is electric field strength. The coefficient d, which links together the stimuli and responses in the above equations, is known as the piezoelectric coefficient. It is the same for the direct and converse effects (albeit with different units), and is of key importance in the study and comparison of piezoelectric materials.

All materials, piezoelectric or not, undergo some (typically, fairly small) change in dimensions upon exposure to an electric field. If this change is proportional to the *square* of the electric field, the effect is known as electrostriction.[10] The piezoelectric effects, on the other hand, show a *linear* proportionality between the applied field (σ, E) and the response (P, ϵ). In addition, all piezoelectric materials show both the direct and the converse effect, whereas the phenomenon of electrostriction has no converse counterpart.

The piezoelectric tensor

The equations given above for the direct and converse piezoelectric effect are only suitable for a qualitative description of the phenomenon. In reality, piezoelectricity is a highly anisotropic property, as are many physical properties of crystals. Both polarization and electric field are vectors, while stress and strain are second-rank tensors (that is, 3×3 matrices). This makes the piezoelectric coefficient d a third-rank tensor, a three-dimensional array which is not so easily displayed on two-dimensional paper. An alternative statement of Equations (2.1) and (2.2) is often given as

$$P_i = d_{ij}\sigma_j \qquad (i = 1,2,3; j = 1,2,\ldots,6) \tag{2.3}$$

$$\epsilon_j = d_{ij}E_i \qquad (i = 1,2,3; j = 1,2,\ldots,6), \tag{2.4}$$

where the six components of stress (σ) and strain (ϵ) take into account both tensile and shear forces in three dimensions, conventionally denoted as in Figure 2.2. The indices 1, 2 and 3 correspond to tensile stress and strain along the x, y and z axes respectively, while 4, 5 and 6 denote shear stress and strain in planes *normal* to the x, y and z axes. In Equations (2.3) and (2.4), summation is implied over the repeated indices (j in (2.3) and i in (2.4)), a convention referred to as Einstein summation notation.[11]

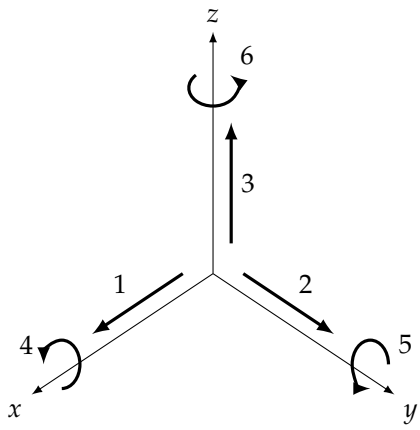

FIGURE 2.2: Definition of subscripts used in Equations (2.3) and (2.4). 1, 2 and 3 denote tensile components along the x, y and z axes, while 4, 5 and 6 denote shear components about the x, y and z axes, respectively.

With this notation, there are 18 coefficients d_{ij} that form a 3×6 matrix $\mathbf{d}$, the piezoelectric matrix of the material. This matrix takes on slightly different forms for different materials, in the sense that some components vanish for certain symmetry classes, making the number of independent piezoelectric coefficients significantly less than 18 in most cases. For instance, crystals belonging to the orthorhombic class $mm2$, such as KNN at room temperature, have only five independent components:

$$\mathbf{d} = \begin{pmatrix} 0 & 0 & 0 & 0 & d_{15} & 0 \\ 0 & 0 & 0 & d_{24} & 0 & 0 \\ d_{31} & d_{32} & d_{33} & 0 & 0 & 0 \end{pmatrix}$$

For crystals in the tetragonal class $4mm$ there are only three independent components. A more detailed explanation of this fact, along with the full tensor equations for piezoelectricity and the justification for representing them in the matrix notation of (2.3) and (2.4), is given in Appendix B.

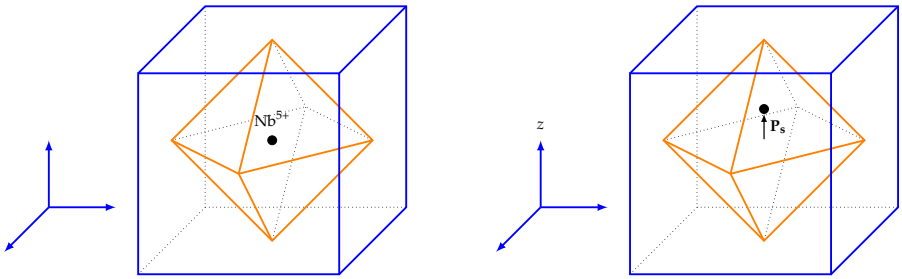

FIGURE 2.3: Origin of spontaneous polarization in KNN: (a) Cubic KNN (high temperature form), with the Nb^{5+} ion situated in the centre of the perovskite unit cell, yielding a non-polar crystal. Alkali ions are situated at the corners of the cube, and oxygen ions at the apices of the octahedron. (b) Tetragonal KNN (intermediate temperature form), with the Nb^{5+} displaced along the $[001]_{pc}$ direction (pseudo-cubic [001] direction, referred to the cubic unit cell), resulting in a spontaneous polarization, $\mathbf{P_s}$, parallel to the z axis.

2.2 Piezoelectric ceramics

Ferroelectricity

In a polycrystalline ceramic body, the grains are oriented more or less randomly, at least if special precautions are not taken. The random orientation of the grains also orients the polar axes of the grains randomly, with the result being that the net polarization of the ceramic becomes zero and the material behaves non-piezoelectrically. A ceramic material can be made piezoelectric, however, if it also has the property of ferroelectricity.

The crystallographic criterion for piezoelectricity is that the material must possess a unique *polar axis*. If a *spontaneous polarization* also exists along this polar axis, the material is said to be pyroelectric, and pyroelectrics thus form a subset of piezoelectrics. The concept of spontaneous polarization is illustrated in Figure 2.2 for the case of KNN, in which the spontaneous polarization arises from displacement of the Nb^{5+} ions with respect to the oxygen sublattice.

In some pyroelectric materials, it is possible to switch the direction of spontaneous polarization by application of an electric field. If this is the case, the material is said to be ferroelectric, and ferroelectric materials thus form a

subset of pyroelectrics. The connection between piezo-, pyro- and ferroelectrics is shown in Figure 2.4. An important distinction in ferroelectrics is that while piezo- and pyroelectricity are properties that directly follow from the crystal structure of the materials, ferroelectricity is a property that must be verified experimentally for each material.[10]

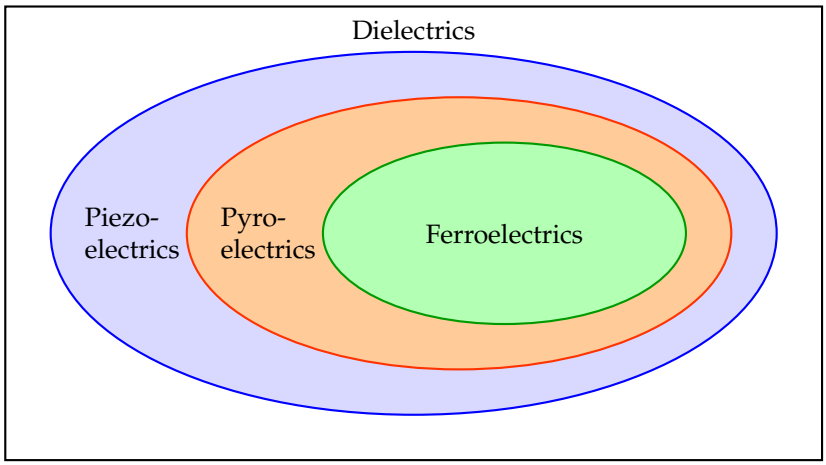

FIGURE 2.4: Relations between piezo-, pyro- and ferroelectrics.

Poling and ferroelectric domains

A polycrystalline ceramic of a piezoelectric material is in principle, as mentioned before, non-piezoelectric, because of the random orientation of grains and therefore of spontaneous polarization. If the material is ferroelectric, however, the direction of spontaneous polarization in a grain can be switched by application of an electric field, and this makes it possible to create a piezoelectric ceramic (piezoceramic).

At this point it is important to explain the concept of *domains*. Domains are regions within the grains of a ferroelectric material, in which the direction of spontaneous polarization is equal. When a spontaneous polarization arises in a crystal (such as when a crystal of KNN is cooled below 400 °C and it goes from the paraelectric to the ferroelectric state), domains of alternating polarization form, so as to reduce the electric field created. This division into domains is illustrated in Figure 2.5.

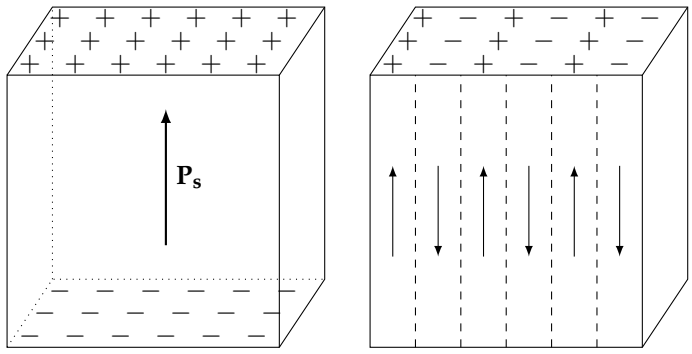

FIGURE 2.5: Principle of domain formation in ferroelectric crystals. A single-domain structure (a) will have a higher energy due to surface charges than a structure consisting of alternating domains (b), which is therefore a more stable form. Dashed lines in (b) represent 180° domain walls. Figure redrawn from Moulson and Herbert.[10]

The domains are separated by *domain walls*, which are regions over which the polarization changes from one direction to another. This is not an abrupt change, but happens gradually over several unit cells of the crystal. Domain walls are classified according to the angle between the polarization directions in the domains they separate, so that a domain wall separating two domains with 180° between the polarization directions will be referred to as a "180° domain wall". This is the kind of domain wall shown in Figure 2.5(b).

During poling of the ceramic, domain walls inside the grains will move. Domains that are well aligned with the applied field will grow at the expense of those that are poorly aligned, and thus a net polarization arises in the ceramic. When non-180° domain walls move (that is, when the polarization of a domain changes by less than 180°), it brings about a change in the physical dimensions of the grain, leading to a strain in the material. This strain will make some of the domains switch back when the electric field is removed, although most will stay in their switched state. This leads to a permanent polarization of the ceramic in the same direction as the applied field, and makes the ceramic behave piezoelectrically.

A poled ceramic belongs to the symmetry class ∞m, that is, it has rotational symmetry about the poling direction, which is the only unique direction in

the material. The piezoelectric matrix of the ∞m class is identical to the one for the $4mm$ class, and has only three independent piezoelectric coefficients: d_{33}, d_{31} and d_{15}. The polar axis is conventionally named z, and referred to with subscript 3 as in Figure 2.2. The x and y directions are two arbitrary orthogonal directions in the plane normal to z. Based on this, the coefficient d_{33}, when referred to a ceramic, describes the polarization developed along the poling direction, when a tensile stress is applied in the same direction (or, equivalently, the tensile strain developed along the poling direction when an electric field is applied in the same direction). In the same way, d_{31} describes the polarization that develops along z when the material is subjected to a tensile stress *normal* to z. The subscripts 4, 5 and 6 are used for shear as shown in Figure 2.2, so d_{15} describes the polarization that develops along x when the material is subjected to shear about the y axis.

Describing piezoelectric performance

When dealing with measurements of piezoelectric performance, it is very important to be aware of the difference between the coefficient d_{33} described above, and the "measured d_{33}", or longitudinal piezoelectric coefficient, d^*_{33}. Both are obtained experimentally by measuring the strain developed in a certain direction in the material, in response to an applied electric field in the same direction. For d_{33}, this direction is by definition the polar axis of the material (the $\langle 110 \rangle_{\mathrm{pc}}$ directions for an orthorhombic crystal such as KNN, illustrated in Figure 2.2). The symbol d^*_{33}, however, is used when the strain and field are in the same direction, but the direction of measurement with respect to the polar axis is not specified. The relationship between them is illustrated in Figure 2.6.

It should be mentioned that measurements of the longitudinal piezoelectric coefficient d^*_{33}, with the field applied normal to the surface of a flat disc like the one in Figure 2.6, is not the only possible "testing regime" for a piezoelectric material. A transverse piezoelectric coefficient can for instance be found by measuring the strain normal to the applied field, and similarly a shear coefficient can be measured. The longitudinal coefficient is, however, the most common of the possible experimental figures, both because it is the simplest to measure and arguably also the most intuitive to understand.

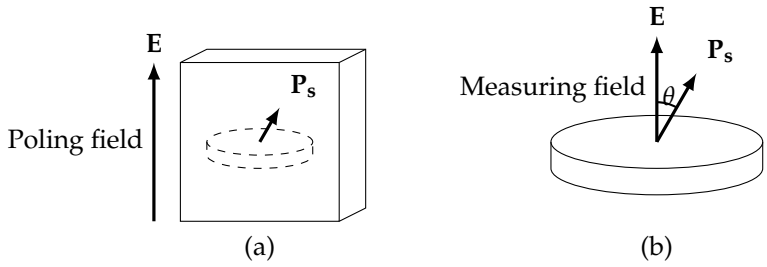

FIGURE 2.6: Difference beween d_{33} and d^*_{33}: (a) A ferroelectric crystal is poled in an electric field, yielding a spontaneous polarization $\mathbf{P_s}$ along a polar direction. An arbitrarily oriented sample is cut from the material for piezoelectric characterisation. (b) Piezoelectric response is measured normal to the sample surface, either by applying an electric field (shown) and measuring displacement, or by applying a force and measuring polarization. d^*_{33} is the measured piezoelectric coefficient in the direction making an angle θ with the direction of spontaneous polarization. When $\theta = 0°$, d^*_{33} = d_{33}.

Rotators and extenders

The longitudinal piezoelectric coefficient d^*_{33} depends on the elements of the piezoelectric matrix of the material, as well as the direction of measurement. One might think that d^*_{33} always shows a maximum when measured along a polar direction in the material, i.e., $\theta = 0$, but this is not necessarily the case, as the following discussion will show. The focus in this section will be on $mm2$ single crystals, and according to Kholkin et al.,[12] for this crystal class, d^*_{33} varies with direction as

$$d^*_{33} = \cos\theta[(d_{31} + d_{15})\sin^2\theta\sin^2\phi + (d_{32} + d_{24})\sin^2\theta\cos^2\phi + d_{33}\cos^2\theta], \tag{2.5}$$

where θ is the angle away from the polar axis as shown in Figure 2.6, and ϕ is the angle of rotation *around* the polar axis. This expression shows that parallel to the polar axis ($\theta = 0°$), the only contribution to d^*_{33} comes from d_{33} itself. If this value is also the maximum value d^*_{33} reaches, the material is termed an *extender ferroelectric*. When measuring in a direction away from the polar axis, however, the longitudinal coefficient also receives a contribution from the transverse coefficients d_{31} and d_{32}, and the shear coefficients d_{15} and d_{24}. If these are large compared to d_{33}, they can dominate and lead to a maximum value for d^*_{33} at some angle away from the polar axis. In this case, the material

is termed a *rotator ferroelectric*.

To analyze these cases in more detail, Equation (2.5) can be rewritten as follows:

$$\frac{d_{33}^*}{d_{33}} = \cos\theta[\cos^2\theta + \sin^2\theta(\gamma_x \sin^2\phi + \gamma_y \cos^2\phi)], \tag{2.6}$$

with the coefficients γ_x and γ_y defining the degree of anisotropy, in the x and y directions respectively, through the relations

$$\gamma_x = \frac{d_{31} + d_{15}}{d_{33}} \tag{2.7}$$

$$\gamma_y = \frac{d_{32} + d_{24}}{d_{33}}. \tag{2.8}$$

Equation (2.6) gives the magnitude of d_{33}^* relative to d_{33} as a function of only the angle away from the polar axis, and the anisotropy ratio.* The most drastic variation in d_{33}^* comes from the variation in θ, due to the cosine term that envelops the term in brackets in Equation (2.5). The variation due to ϕ depends on the difference between γ_x and γ_y, which may not necessarily be large. In the limiting case where $\gamma_x = \gamma_y$, d_{33}^* achieves conical symmetry with respect to the polar axis, and becomes independent of ϕ. This happens when KNN is heated to above 200 °C and transforms into the $4mm$ tetragonal structure.

A plot of Equation (2.6) with $\phi = $ const. is shown in Figure 2.7. The value of γ will vary slightly with ϕ, but the general shape of the curve will be as shown, with a maximum value for d_{33}^* for some angle away from the polar axis if the anisotropy ratio is higher than 1.5.

Figure 2.7 sheds light on several important aspects of d_{33}^*. As was stated before, it can be seen that parallel to the polar axis ($\theta = 0$), d_{33}^* is equal to d_{33}, so the ratio between them is 1. Also, there is no longitudinal piezoelectric response in the direction normal to the polar axis ($\theta = 90°$). These boundary conditions are valid for all $mm2$ crystals, but at intermediate angles, materials behave differently depending on their piezoelectric anisotropy.

For materials with an anisotropy coefficient of 1.5 or less (extenders), the value $d_{33}^* = d_{33}$ at $\theta = 0$ is also the maximum value. However, for materials with an anisotropy coefficient greater than 1.5 (rotators), d_{33}^* passes through a maximum at some intermediate angle between 0° and 90°. Furthermore, this

*In the literature, the "anisotropy ratio" of a piezoelectric material is usually defined as d_{15}/d_{33}, disregarding both the coefficient d_{31}, which is usually small, and the variation in anisotropy by rotation through ϕ. The definition used here is chosen to correspond to the analytical expression for d_{33}^*.

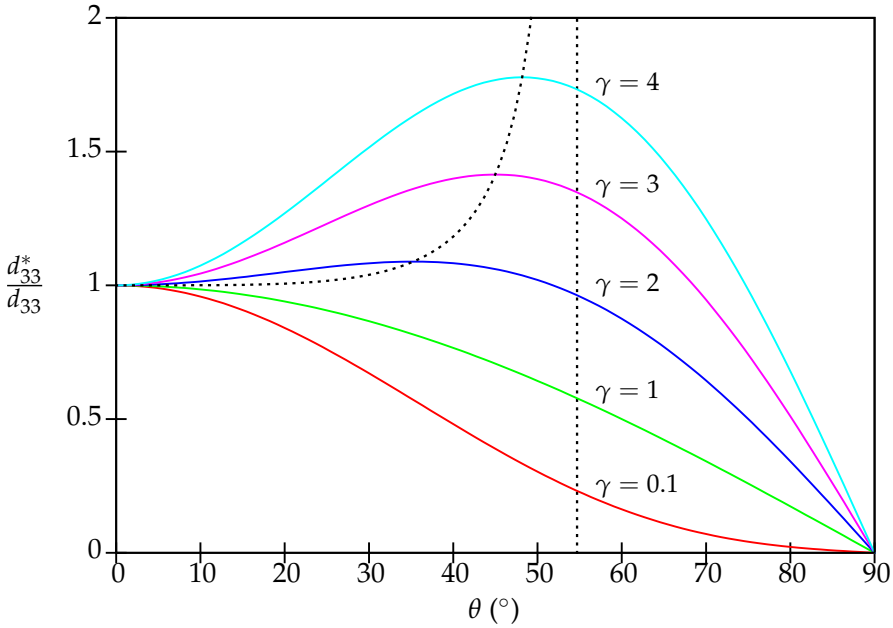

FIGURE 2.7: Variation of longitudinal piezoelectric coefficient as a function of angle away from the polar axis in an $mm2$ crystal. Curves corresponding to different anisotropy ratios are shown. The dashed black curve shows how the location of maximum d^*_{33} moves away from the polar axis with increasing piezoelectric anisotropy, approaching a limit value of 54.7° (vertical dashed line).

maximum shifts towards higher angles as the anisotropy increases, for example, an anisotropy of $\gamma = 2$ gives an optimal angle of $\theta = 35.2°$, while $\gamma = 3$ gives $\theta = 45°$. It can be shown mathematically that the angle of maximum d^*_{33} in an $mm2$ crystal tends towards the value 54.7° as the anisotropy ratio increases. This angle corresponds to the "rhombohedral angle" (the angle between the directions [001] and [111] in a cubic system), and is indicated by a dashed vertical line in Figure 2.7.

As stated above, this discussion applies to KNN single crystals, and is not directly transferable to ceramics. This means that while the piezoelectric response of a KNN single crystal is governed by Equation (2.5), the piezoelectric response of a ceramic is much more complicated and does not lend itself to an

exact mathematical treatment. A thorough understanding of the anisotropic behaviour of single crystals, especially with regards to extender versus rotator behaviour, is nevertheless of key importance for understanding the concept of crystallographic texturing, as will be described later.

2.3 Sodium potassium niobate

Overview of the KNN system

Sodium potassium niobate, $K_{1-x}Na_xNbO_3$ (KNN), is a ferroelectric perovskite that can be regarded as a solid solution of potassium niobate, $KNbO_3$ (KN), and sodium niobate, $NaNbO_3$ (NN). The term KNN is used in reference to various compositions between the two end members KN and NN, although here "KNN" will mean the composition corresponding to $x = 0.5$ unless otherwise is specified.

KNN was discovered to be piezoelectric over 50 years ago,[13] and received considerable attention in the classic book on piezoceramics by Jaffe et al.[2] The KNN system was reported as showing a peak in piezoelectric properties at the composition corresponding to 47.5 % KN,[2] but as this peak is broad, the 50 % composition has often been chosen for simplicity.

Structure and properties

Upon cooling from high temperature, KNN undergoes several phase transitions. These transitions are the same as for the end member KN, although at slightly different temperatures. A phase diagram of the pseudo-binary NN–KN system is given in Figure 2.8, and shows that at temperatures above approximately 400 °C, KNN is cubic and paraelectric with point group $m\bar{3}m$, with the unit cell that was shown in Figure 2.2(a). Between approximately 400 °C and 200 °C, it is tetragonal and ferroelectric with point group $4mm$, and the unit cell that was shown in Figure 2.2(b). Below 200 °C and down to well below room temperature, KNN is orthorhombic, with point group m (monoclinic) or $mm2$ (orthorhombic) depending on composition.

The two room-temperature phases m and $mm2$ are separated by a vertical line at around $x = 0.5$ in the phase diagram, meaning that the transition between the two phases depends mainly on the composition of the material, and very little on temperature (given that it is below 200 °C). This is an example of a *morphotropic phase boundary* (MPB). In contrast, phase boundaries depending mainly on temperature and very little on composition, thus appearing as

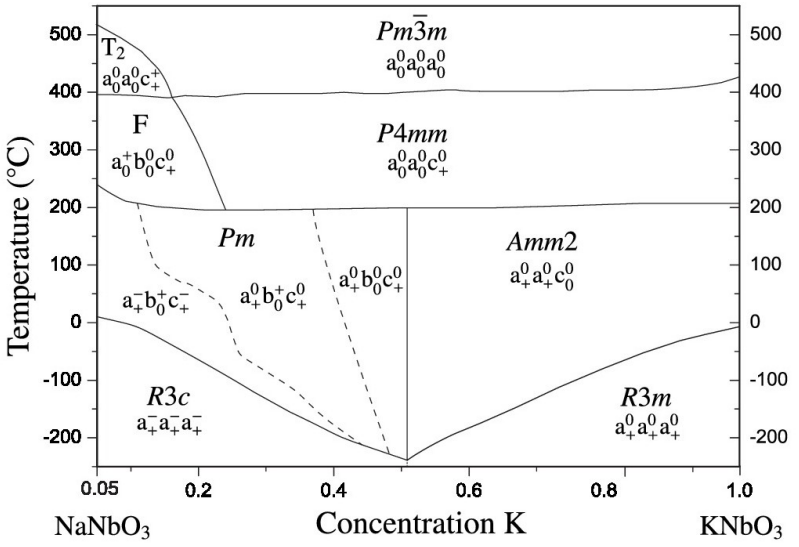

FIGURE 2.8: Phase diagram of the NN–KN system, from Baker.[14] Note that the section closest to pure NN is not included.

horizontal lines in the phase diagram, are termed *polymorphic phase boundaries* (PPB). An example of this is the cubic-tetragonal phase boundary of KNN at around 400 °C. Materials possessing MPBs are of great interest in piezoceramics reasearch, as piezoelectric properties are known to reach peak values in the vicinity of such phase boundaries, an example being the very good piezoelectric properties for compositions in the $PbZrO_3$–$PbTiO_3$ (PZT) system.[10]

Chemical modifications: KNNLT

Pure KNN does not show sufficiently good piezoelectric properties to be able to compete with commercial piezoelectrics such as PZT. Therefore, several attempts have been made to tailor the properties of KNN by chemical modifications. According to the review article by Rödel et al.,[4] these generally fall into two categories: Those that attempt to improve the sintering properties of KNN while retaining the basic structure and phases shown in Figure 2.8; and those who modify the material such that the phase boundaries are shifted in a

beneficial way.

One of the most studied variations of the KNN system, which belongs to the class of modifications to the phase diagram, is the composition $(Li_xK_yNa_{1-x-y})$-$(Ta_zNb_{1-z})O_3$, or KNNLT. In these compositions, lithium is substituted for sodium or potassium on the perovskite A site, and tantalum for niobium on the B site. Generally, the fraction of lithium is in the range 3–7 at% and the fraction of tantalum in the range 10–20 at%,[15] but pseudo-binary compositions between KNN and $LiTaO_3$ have also been investigated.[16] In any case, the ratio between sodium and potassium is open for adjustment, but is generally close to 1:1 or slightly towards the sodium-rich side, as for pure KNN compositions.

Structurally, KNNLT is similar to KNN, while properties such as piezoelectric performance and phase transition temperatures are slightly different. The role of lithium and tantalum in KNNLT can be summarized as follows:[4] tantalum hinders abnormal grain growth during sintering, and decreases the temperatures for both the orthorhombic–tetragonal (O–T) transition and the ferroelectric-paraelectric transition (the Curie temperature T_C). By bringing the O–T transition, a polymorphic phase transition in the KNN system, closer to room temperature, the room temperature piezoelectric properties are enhanced. Lithium also contributes to lowering the O–T transition towards room temperature, while simultaneously increasing T_C and increasing the densification during sintering. The different phase transition temperatures are listed in Table 2.1 for typical KNN and KNNLT compositions.

TABLE 2.1: Phase transition temperatures of KNN and KNNLT-related modifications. The latter includes both compositions with Li as the only dopant, and compositions with both Li, Ta and Sb, showing the large variations made possible by doping.

Material	T_{O-T} °C	T_C °C	Ref.
KNN	∼200	∼400	14
KNNLT-related	15–50	253–475	4

2.4 Processing of KNN-based ceramics

Sintering

Sintering of KNN-based materials is challenging in several ways. The review article by Rödel et al.[4] specifically mentions four critical issues in processing

of KNN materials by conventional solid state methods, where the most significant is poor densification. The other issues discussed are compositional inhomogeneity, especially upon chemical modification by introduction of new elements, phase stability at high temperatures, and volatility of the alkali oxides, all of which represent challenges when sintering the materials.

Poor densification of KNN can be helped through the use of different sintering aids. Copper compounds, in the form of either oxides or compounds with alkali metals and niobium, are frequently used in KNN-based systems,[5,17,18] but other sintering aids have been demonstrated as well.[19] In the author's specialization project during the autumn of 2011,[6] manganese(II) oxide was added to KNN and shown to lower the sintering temperature and increase the density of the ceramics. Addition of manganese oxide has also been reported to decrease leakage current, increase dielectric permittivity and reduce dielectric loss in KNN thin films,[20] making it a promising sintering aid for KNN materials.

The end members of the pseudo-binary KNN system, KN and NN, melt at temperatures around 1090 °C and 1420 °C, respectively.[21] The melting point of KNN is located around 1110 °C, which is close to the sintering temperatures usually reported for KNN. Several reports show that there is a quite narrow temperature window within which KNN sinters adequately, with a steep increase in density upon approaching the optimal sintering temperature, and a decrease upon exceeding it.[19,22,23] Attempts at explaining this have traditionally incorporated the phenomenon of alkali volatilization, by which the material is partially depleted of alkali oxides according to equilibria such as the following for potassium:

$$\mathrm{K_2O(s)} \rightleftharpoons 2\,\mathrm{K(g)} + \tfrac{1}{2}\,\mathrm{O_2(g)}, \tag{2.9}$$

possibly involving other oxide species, and similarly for sodium. This leads to non-stoichiometry, which promotes formation of alkali-deficient secondary phases of tungsten-bronze structure, which leads to abnormal grain growth and a non-uniform microstructure.[24] More recently, however, it has also been suggested that sintering of KNN at too high temperatures leads to the formation of a liquid phase, which again leads to compositional segregation of the material due to the solidus line in the binary phase diagram being almost horizontal.[21,25] The reason for the narrow range of suitable sintering temperatures for KNN-based materials is therefore not yet fully understood, and might involve several different phenomena.

Texturing

Crystallographic texturing is the process of making a dense ceramic with a non-random distribution of grain orientations. This is often done by introducing *template particles* in the ceramic powder. These are particles of anisometric shape, which can therefore be oriented mechanically during green body shaping. During sintering, these oriented particles will grow at the expense of the fine-grained powder particles, in a form of Ostwald ripening generally referred to as *templated grain growth* (TGG). The crystallographic orientation of the template particles will direct the further grain growth during sintering, which leads to a preferred orientation of the grains in the dense ceramic. The underlying idea is that a textured ceramic is more "single crystal-like" than a non-textured one, which in turn can be beneficial for functional properties such as piezoelectricity.

The best known example of texturing within the KNN family of materials is probably the work by Saito et al.[5] In this work, the composition $(K_{0.44}Na_{0.52}Li_{0.04})(Nb_{0.84}Ta_{0.10}Sb_{0.06})O_3$, a composition known as LF4, was textured with (001)-oriented platelets of $NaNbO_3$, achieving an increase in d_{33} from $300\,\mathrm{pC\,N^{-1}}$ to $416\,\mathrm{pC\,N^{-1}}$.

The texturing procedure used in this work is based on the one developed by Madaro.[9] The method consists of producing thick films of KNN by tape casting, using needle-shaped KNN template particles that are aligned parallel to the casting direction. Pieces of the tape are then cut out and stacked vertically, before being pressed and sintered. The process is shown schematically in Figure 2.9.

The template particles utilized here have been reported to grow in the $[100]_{\mathrm{pc}}$ direction (that is, the pseudo-cubic [100] crystallographic direction is parallel to the long axis of the templates; see Appendix A for an explanation of crystallographic directions and the $[uvw]_{\mathrm{pc}}$ notation).[27] This is illustrated in Figure 2.10(a), which shows how possible polarization directions relate to the shape of the template. During the casting step, the templates are aligned in two ways, in the sense that they lie both in the plane of the tape, and also parallel to the casting direction. However, the particles still have a rotational degree of freedom along their length axis, as shown in Figure 2.10(b).

The difference between the texturing method of Saito et al., and the texturing method used in this work, is illustrated schematically in Figure 2.11. The figure shows a comparison between (001)-texturing, as used by Saito and others, where the [001] direction is normal to the tape casting plane; and $(hk0)$-texturing, where the [001] direction is parallel to the tape casting direction. In

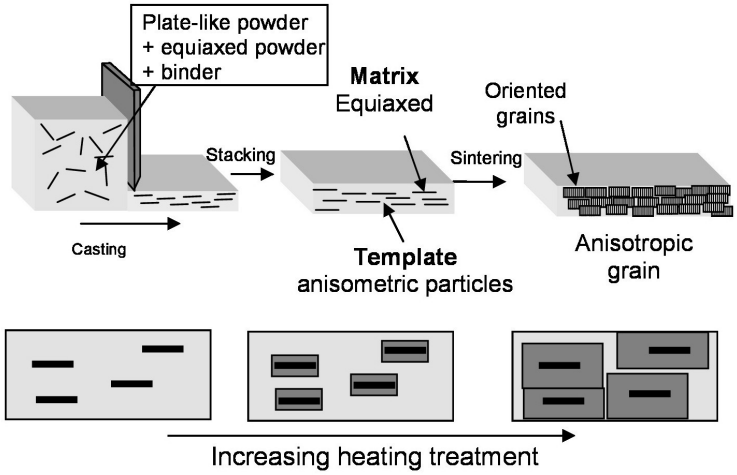

FIGURE 2.9: Illustration of the texturing procedure. Top row shows tape casting, lamination of tape and sintering. Bottom row illustrates the templated grain growth process during the sintering step. Illustration from Madaro,[9] based on Messing.[26]

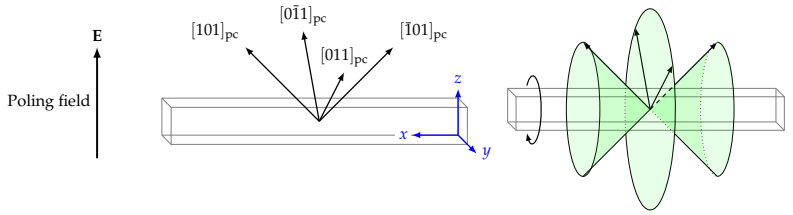

FIGURE 2.10: KNN templates shown schematically. (a) Possible directions of spontaneous polarization (polar axes) in a template particle poled in the $[001]_{pc}$ direction. (b) Illustration of how polar axes move when a template rotates freely around its long axis. The polar axes lie on two cones with an opening angle of 90°, and on a disc normal to the long axis of the template. No polarization vectors lie parallel to the template itself.

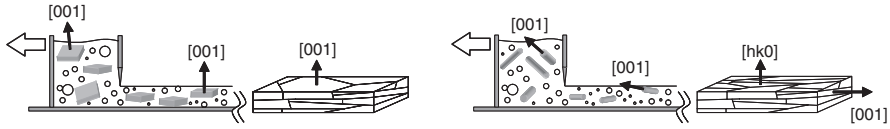

FIGURE 2.11: Difference between (a) (001)-texturing, used by Saito[5] and others, and (b) (hk0)-texturing, similar to the (0kl)-texturing used in this work. Figure from Jones.[28]

this work, it is the [100] direction that is parallel to the tape casting direction, leading to $(0kl)$-textured tapes. In addition to this "crystallographic difference", there is a difference with respect to chemistry, in that the work of Saito et al. included the use of $NaNbO_3$ templates in a KNNLTS matrix, while in this work the templates are made from KNN.

As was mentioned earlier, the piezoelectric anisotropy of a material must be understood if one is to perform texturing in a beneficial way. Specifically, it is important to know whether the material in question is an extender or rotator ferroelectric, or a borderline material in this respect. In the case of an extender ferroelectric, the goal of texturing is to be able to pole a larger number of grains along a polar axis, thus increasing the poling efficiency. In the case of a rotator ferroelectric, on the other hand, the goal is to end up with a large number of polar axes at some non-zero angle to the poling field, where the optimal angle is governed by Equation (2.5). This has the effect of increasing piezoelectric response by utilizing the large shear coefficients (d_{15} and d_{24}) of rotator ferroelectrics.

In the specific case of KNN, not all piezoelectric coefficients are known. A selection of piezoelectric coefficients published on KNN and KNN-related materials is given in Table 2.2, along with calculated anisotropy ratio in each case. To the best of the author's knowledge, no detailed piezoelectric data exists for KNN single crystals. The data for KNN ceramics varies somewhat, but generally shows a low degree of anisotropy, which is to be expected from non-textured ceramics. A textured ceramic, however, retains the anisotropy of the single-crystal grains to a greater extent than a non-textured material, a concept that is illustrated in Figure 2.12. For this reason, textured materials are sometimes described as having "single crystal-like" properties.

Due to the lack of data on the piezoelectric coefficients of KNN single crystals, it is not known whether KNN is an extender or a rotator ferroelectric, although certain estimates can be made. If one can assume that the connection

TABLE 2.2: Piezoelectric coefficients for KNN and KNN-related materials, along with calculated anisotropy ratio γ in each case. For single crystals, γ is given as the range γ_x–γ_y, as found from Equation (2.8).

Material (point group)	Piezoelectric coefficient (pC N^{-1})					γ	Ref.
	d_{31}	d_{32}	d_{33}	d_{24}	d_{15}		
Single crystals ($mm2$)							
KN	9.8	-19.5	29.3	156	206	4.7–7.4	29
KN	9.5	-24.6	21.6	205.1	241.5	8.4–10.4	30
Ceramics (∞m)							
KN–0.1Mn	-29.7		80.8		169	1.7	31
KNN	-51		127		306	2.0	32
KNN	-28		84		189	1.9	23
KNNL2–0.45CuO	-33		93		207	1.9	23
KLNN–Cu	-33		102		155	1.2	33
KNN	–		95		168	–	34
KNN–KCN	–		110		162	–	34

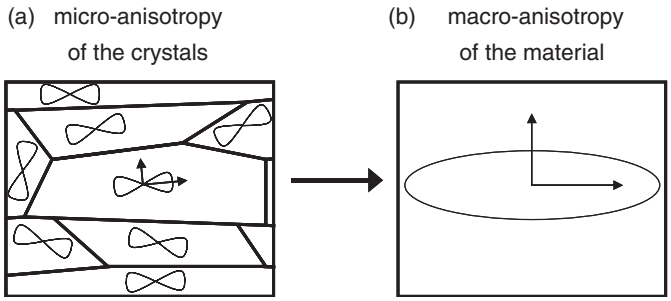

FIGURE 2.12: Relation between micro-anisotropy of the crystalline grains, and macro-anisotropy of a textured ceramic material. Figure by H.J. Bunge and R.A. Schwarzer, adapted from Jones.[28]

between single-crystal and ceramic anisotropy of KNN mirrors that of KN, Table 2.2 indicates that single crystal KNN might be at least as anisotropic as single crystal KN, and therefore a rotator. Another indication comes from the results obtained by Saito et al.,[5] which indicates that KNNLTS is a rotator. In said work, (001)-textured KNNLTS was considered, meaning that the template particles were oriented so that the $[001]_{\mathrm{pc}}$ direction was normal to the surface of the ceramic sample, and thus parallel to the poling direction. Since the polar directions of orthorhombic KNN are the $\langle 110 \rangle$ directions, (001)-texturing ensures that an increased number of grains have their polar axes at 45° to the poling direction. Based on the significant increase in d_{33} obtained by texturing in this case (from 300 pC N^{-1} to 416 pC N^{-1}), it is very likely that KNNLTS is a rotator ferroelectric.

To achieve the same effect with $(0kl)$-textured materials, which is the result of aligning $[100]$-grown needle-shaped template particles with the tape casting direction, one would need to pole the material along the tape casting direction. This would ensure that an increased number of polar directions in the material lie at a 45° angle to the poling field. Figure 2.10(b) illustrates how the polar directions of the template particles are distributed when the template particle rotates freely, and it can be seen that the longitudinal direction of the template is the optimal poling direction for achieving high piezoelectric response, given that the material is a rotator ferroelectric.

Chapter 3

Experimental work

3.1 Sample compositions

The different KNN and KNNLT compositions used during this work are listed in Table 3.1, with chemical formulae and the abbreviations that are used throughout this text.

3.2 Powder preparation

Powder of KNN was prepared by spray pyrolysis according to the procedure developed by Madaro.[9] The synthesis followed the "niobium ammonium oxalate route", in which an aqueous precursor solution containing sodium nitrate, potassium nitrate and niobium ammonium oxalate was spray pyrolysed at 1000 °C and subsequently calcined for 6 hours at 800 °C. The powder was

TABLE 3.1: Chemical formulae and abbreviations for the KNN and KNNLT samples studied in this work.

Formula	Abbreviation
$K_{0.5}Na_{0.5}NbO_3$	KNN
$K_{0.5}Na_{0.5}NbO_3$ + 0.5 mol% MnO	KNN-Mn
$(K_{0.46}Na_{0.54})_{0.97}Li_{0.03}Nb_{0.81}Ta_{0.19}O_3$	KNNLT
$((K_{0.46}Na_{0.54})_{0.97}Li_{0.03})_{0.995}Mn_{0.005}Nb_{0.81}Ta_{0.19}O_3$	KNNLT-Mn(A)
$(K_{0.46}Na_{0.54})_{0.97}Li_{0.03}(Nb_{0.81}Ta_{0.19})_{0.995}Mn_{0.005}O_3$	KNNLT-Mn(B)

planetary milled for 30 minutes using zirconia milling balls, and finally sieved at 250 µm.

KNN-Mn powder was prepared by mixing KNN powder with an aqueous solution of manganese(II) nitrate ($Mn(NO_3)_2$). The water was evaporated under a reduced pressure of 55 mbar and a temperature of 55 °C. The powder was calcined again at 600 °C for 6 hours, and finally mortared and sieved at 250 µm.

Powders of KNNLT, KNNLT-Mn(A) and KNNLT-Mn(B) (CerPoTech AS, Trondheim, Norway) were delivered according to the compositions listed in Table 3.1. The powders had been prepared by spray pyrolysis, calcined at 600 °C and sifted at 250 µm, so no further preparation of the powders was needed.

Template particles of KNN were prepared as described by Madaro[27] using molten salt conversion of $K_2Nb_4O_{11}$. Anisometric particles of $K_2Nb_4O_{11}$ were mixed with a stoichiometric amount of Na_2CO_3 according to the reaction

$$K_2Nb_4O_{11} + 2\,NaCO_3 \xrightarrow{KCl} 4\,K_{0.5}Na_{0.5}NbO_3 + CO_2(g), \tag{3.1}$$

with KCl used as a flux agent. The mixture was heated in an alumina crucible to 830 °C for 30 minutes with heating and cooling rates of 200 °C h^{-1}. Afterwards, the salt/oxide mixture was dissolved in distilled water, and the KNN template particles were isolated by using a Millipore vacuum filtering system with 0.45 µm filters. The template particles were finally dried at 200 °C for a few hours.

3.3 Investigation of sintering behaviour

Dilatometry

As a first approach to optimizing the sintering program, all powders were studied by dilatometry using a Netsch 402C dilatometer (Selb, Germany). The KNN and KNN-Mn powders were heated to 1100 °C with a heating rate of 10 °C min^{-1}, while the KNNLT powders were heated to 1110 °C with a rate of 5 °C min^{-1}. An atmosphere of synthetic air was used for all dilatometry experiments.

Isothermal sintering

Based on the dilatometer studies, isothermal sintering of KNNLT samples was performed. Pellets of 10 mm diameter and a thickness of 1 mm to 2 mm

TABLE 3.2: Composition of slurry used for tape casting of KNN-Mn and KNNLT-Mn(A). 10 g of powder (matrix + templates) was used in each batch.

Compound	Function	Amount (wt%)
KNN-Mn/KNNLT-Mn(A)	Matrix powder	26.6–26.7
KNN	Templates	3.0
Distilled water	Solvent	35.4–35.7
Darvan C	Dispersion agent	0.1–0.2
PVA (15 wt% solution)	Binder	33.5–33.7
PEG	Plasticizer	0.8–0.9
PPG	Defoamer	0.2–0.3

were uniaxially pressed and sintered for 1 hour at different temperatures, with heating and cooling rates of 200 °C h^{-1}. During sintering, the pellets were placed on a bed of coarse KNN powder inside an alumina crucible with lid, so as to minimize possible evaporation of alkali compounds.

Similar studies of KNN, both pure and with additions of copper oxide and maganese oxide, have been performed previously by the author, including compositions identical to the KNN-Mn powder used in this work.[6] A separate investigation of the sintering properties of KNN-Mn was therefore not performed here.

3.4 Preconsolidation and sintering

Tape casting

Tape casting was used to prepare thick films of KNN-Mn and KNNLT-Mn(A), according to the procedure given by Madaro.[9] A slurry was made, containing the fine-grained powders, distilled water and Darvan C, with composition given in Table 3.2. These components were mixed using a ball mill with zirconia balls for 5–6 hours, after which the PVA binder, PEG and PPG were added. The slurry was further mixed for 16–24 hours before the KNN template particles were added. The slurry was then stirred carefully for 3 hours using a magnetic stirrer at low speed, so as not to damage the template particles. After this step, the slurry was de-aired by first being held for 30 minutes in an ultrasound bath, and then for 10 minutes in a vacuum desiccator at 25 mbar. Finally, the slurry was aged for 30 minutes at ambient temperature and pressure.

A tape was cast from the slurry using a tabletop tape caster (Richard E. Mistler Inc., USA) with Mylar film as the carrier substrate. A special gated doctor blade was used to align the template particles during casting. The cast tape was left to dry in air at ambient temperature.

Preparation of textured samples

The textured tapes were used to prepare textured samples for piezoelectric characterization. Pieces of 1.0 cm × 1.5 cm were cut from the tape, and stacked top-to-bottom in 40 layers. The stack was laminated in a hot press at a temperature of 70 °C, using a pressure of 30 MPa for 10 minutes. After this, a binder burnout treatment was performed by heating the sample to 600 °C for 6 hours, with a heating rate of 25 °C h^{-1} up to 180 °C, and then 12 °C h^{-1} up to the set point. The cooling rate was 200 °C h^{-1}.

Sintering of the textured laminates was done in a tube furnace (Entech ETF 30-50/17S, Sweden) using an atmosphere of flowing pure oxygen. The heating and cooling rates were 300 °C h^{-1}, with a set point of 1130 °C for the KNN-Mn samples and 1150 °C for the KNNLT-Mn(A) samples. The samples were held at the set point for 14 hours, in order to achieve necessary densification and templated grain growth/texture development when including the relatively large template particles.

After sintering, the density of the laminated samples was measured by Archimedes' method[35] with isopropanol as immersion fluid.

Before piezoelectric characterization, the laminated samples were reduced to a square shape of approximately 5 mm × 5 mm, and about 100 µm to 200 µm of material was grinded off of each side, yielding samples of 500 µm to 800 µm thickness. The grinding was done using #1200 grit SiC paper, with a final grinding/polishing step using #4000 grit SiC paper to achieve a smooth surface. The top and bottom of the samples were coated with silver paste, using a mask of Scotch tape to protect the edges. The silver electrodes were dried for a few minutes, and then hardened by heating the sample to 200 °C for a few hours. After this stage, samples were stored in a desiccator to avoid possible reactions with moisture.

Preparation of non-textured samples

Non-textured samples for piezoelectric characterization were prepared directly from the KNN-Mn and KNNLT-Mn(A) powders. The powders were pressed into pellets of 10 mm diameter and 1 mm to 2 mm thickness. Two different

sintering programs were used for the non-textured samples: one where the pellets were sintered along with, and under the same conditions as, the textured samples, i.e., 14 hours in oxygen atmosphere; and one where the pellets were sintered for just 3 hours in air. Density measurements, grinding/polishing and electroding was done in the same way as for the textured samples.

3.5 Texture analysis

To analyze the degree of texture in the samples, the Lotgering method[36] was used. Grinding and polishing of the samples was done in the same manner as before application of electrodes, in order to ensure that the real bulk material was being investigated. X-ray diffractograms were collected from the samples in the 2θ range 10°–60° using two diffractometers: a Bruker AXS D8 Focus (Karlsruhe, Germany) equipped with a LynxEye PSD, and a Siemens D5005 (Germany) equipped with a Braun PSD. The scans were done using a step size of 0.02°.

The degree of texture was taken as the Lotgering factor, f, which is calculated as follows:[36]

$$f = \frac{p - p_0}{1 - p_0} \tag{3.2}$$

$$p = \frac{\sum_{(100),(011)} I}{\sum_{(hkl)} I} \tag{3.3}$$

$$p_0 = \frac{\sum_{(100),(011)} I_0}{\sum_{(hkl)} I_0}, \tag{3.4}$$

where I is the intensity (height) of a diffraction line in the textured sample, and I_0 the intensity of the corresponding diffraction line in the non-textured reference sample. The (100) and (011) diffraction lines, indexed to $Amm2$ symmetry, are equivalent to the three pseudo-cubic (100), (010) and (001) diffraction lines. The quantity p can be interpreted as the "fractional intensity" of the enhanced (011) and (100) diffraction lines relative to the intensity of the entire diffraction pattern (including the enhanced lines), while p_0 is the corresponding figure for the non-textured reference. The Lotgering factor f will then be a number between 0 and 1, where $f = 0$ corresponds to no enhancement of the chosen diffraction lines at all ($p = p_0$), and $f = 1$ corresponds to all diffraction lines other than the enhanced ones being extinct ($p = 1$). The factor f is thought to be an estimation of the volume fraction of textured material.[26]

3.6 Piezoelectric and dielectric characterization

Equipment and measuring procedure

Piezoelectric characterization was done using an aixACCT TF Analyzer 2000 (Aachen, Germany). The instrument is capable of applying unipolar or bipolar electric fields to a sample, and can detect electric polarization and mechanical displacement at the same time.

The measurement procedure consisted of the following steps:

1. Application of bipolar electric fields with amplitudes from $5\,\mathrm{kV\,cm^{-1}}$ up to $40\,\mathrm{kV\,cm^{-1}}$ in steps of $5\,\mathrm{kV\,cm^{-1}}$. 3–4 cycles were done for each field strength, in order to obtain closed hysteresis loops.

2. Application of unipolar electric fields with amplitudes from $40\,\mathrm{kV\,cm^{-1}}$ down to $5\,\mathrm{kV\,cm^{-1}}$ in steps of $5\,\mathrm{kV\,cm^{-1}}$. 10–15 cycles were done for each field strength, in order to obtain stable values for the average converse piezoelectric coefficient d_{33av}.

3. Poling by heating to 100 °C, application of an electric field of $20\,\mathrm{kV\,cm^{-1}}$, and cooling to below 30 °C while maintaining the electric field. This was followed by aging for 1–2 days.

4. Application of unipolar electric fields from $5\,\mathrm{kV\,cm^{-1}}$ up to $40\,\mathrm{kV\,cm^{-1}}$ in steps of $5\,\mathrm{kV\,cm^{-1}}$. As with the measurements done before poling, 10–15 cycles were done for each field strength.

Piezoelectric coefficient

The piezoelectric characterization equipment used in this work uses the converse piezoelectric effect, and detects mechanical displacement in response to the application of an electric field. The piezoelectric performance is reported as the coefficient d_{33av}, the *average converse piezoelectric coefficient*, which is the slope of a regression line fitted to the unipolar strain–electric field loop.

For each temperature or electric field, 10–15 measurements of d_{33av} were done, in order to reduce the effect of random fluctuations in the measurements. The uncertainty in the measurements was taken to be the sample standard deviation of the measurements.

Temperature dependence of piezoelectric performance

The effect of temperature on piezoelectric performance was investigated for a non-textured KNNLT-Mn(A) sample. The justification for this is that the O–T phase transition in KNNLT lies close to room temperature, while in KNN it is around 200 °C.

15 measurements of d_{33av} were performed for each of a range of temperatures between 25 °C and 100 °C both on heating and cooling. First, the sample was heated from 25 °C to 100 °C, with piezoelectric measurements done for each step of 25 °C. The sample was then cooled, with several measurements done with step sizes of 2.5 °C to 5 °C between 70 °C and 50 °C.

Dielectric spectroscopy

Dielectric spectroscopy was performed on a non-textured sample from each of the two materials KNN-Mn and KNNLT-Mn(A) using a Novocontrol Alpha-A analyzer (Hundsangen, Germany). Both samples had been sintered for 3 hours at their optimal sintering temperature, obtaining relative densities of 92.0 % and 95.7 %, respectively. Sample preparation was done in the same way as for piezoelectric characterization, with silver paste used for electrodes.

For both samples, measurements were done in the temperature range 25 °C to 400 °C, using a heating rate of 2 °C min^{-1}. Measurement sweeps were done every 30 seconds during heating, at frequencies of 1 Hz to 1 MHz, logarithmically spaced. The output of the measurements was relative permittivity and dielectric loss, where the dielectric loss can be interpreted as the ratio between the imaginary and real parts of the permittivity:

$$\tan\delta = \frac{\epsilon_{\mathrm{r}}''}{\epsilon_{\mathrm{r}}'}, \tag{3.5}$$

with $\epsilon_{\mathrm{r}}^{*} = \epsilon_{\mathrm{r}}' + j\epsilon_{\mathrm{r}}''$ being the complex permittivity of the material ($j^2 = -1$). The dielectric loss, $\tan\delta$, is proportional to the electrical energy that is dissipated as heat from the electric component.[10]

The real part of permittivity of KNNLT-Mn(A) at temperatures above the Curie temperature was fitted to the Curie–Weiss law:[10,37]

$$\epsilon_{\mathrm{r}}' = \frac{C}{T-\theta}, \tag{3.6}$$

where C is the Curie constant of the material, and θ is the Curie–Weiss temperature. The latter is usually close to, but not identical to, the Curie temperature T_{c} of the material.

For the KNNLT-Mn(A) sample, an additional measurement was made between room temperature and 100 °C, with heating done in steps and the temperature stabilized before each sweep. This additional measurement was done to complement the piezoelectric measurements done at different temperatures up to 100 °C.

Chapter 4

Results

4.1 Powder characterization

Morphology

Figure 4.1 shows SEM micrographs of the powders used for preparation of samples in this work. The KNNLT-Mn(A) powder seems to consist mainly of flake-like particles, while the KNN powder consists of more cube-like particles.

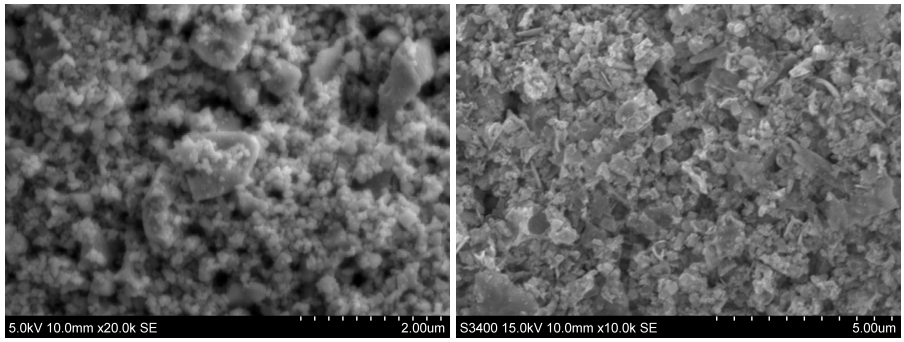

(a) (b)

FIGURE 4.1: SEM micrographs of powders used: (a) KNN, (b) KNNLT-Mn(A). Notice different scale bars.

Sintering behaviour

Shrinkage of powders, as measured by dilatometry, is shown in Figures 4.2 and 4.3 for KNN and KNNLT compositions, respectively. The graphs are drawn to the same scale. Green density of dilatometer samples is given in Table 4.1.

The KNN-Mn powder (Figure 4.2) shows a slightly earlier onset of densification than pure KNN, with a more "bimodal" shrinkage rate curve. Nevertheless, both KNN and KNN-Mn behave very similarly at the maximum temperature with respect to both shrinkage and shrinkage rate.

The KNNLT-Mn(A) (Figure 4.3) shows an earlier onset of densification with respect to the pure KNNLT, while it is the other way around for the KNNLT-Mn(B). Both KNNLT and KNNLT-Mn(A) can be seen to have reached more or less full density at the end temperature, as can easily be seen from the shrinkage rate curves, with the KNNLT-Mn(A) reaching slightly higher density than KNNLT. In contrast, the KNNLT-Mn(B) is still densifying at a high rate at 1110 °C. All KNNLT compositions in Figure 4.3 can be seen to reach significantly higher densities than the KNN compositions in Figure 4.2.

The measured density of isothermally sintered KNNLT samples is displayed in Figure 4.4. From the graph it can be seen that KNNLT-Mn(A) reaches the highest density of all samples, and has an optimal sintering temperature of 1150 °C. For most temperatures, both Mn-doped compositions sinter to higher denisities than the pure KNNLT, but the pure material does not pass through a maximum density in the temperature interval that was investigated. The maximum of KNNLT-Mn(A) at 1150 °C lead to the decision to use this composition for further studies.

TABLE 4.1: Summary of dilatometer data, including green and final density of samples. All densities found by geometrical measurements.

Composition	Heating rate ($^\circ$C min^{-1})	Max. temp. ($^\circ$C)	Density (%)	
			Green	Sintered
KNN	10	1100	60	93
KNN-Mn	10	1100	59	93
KNNLT	5	1110	42	92
KNNLT-Mn(A)	5	1110	44	96
KNNLT-Mn(B)	5	1110	45	89

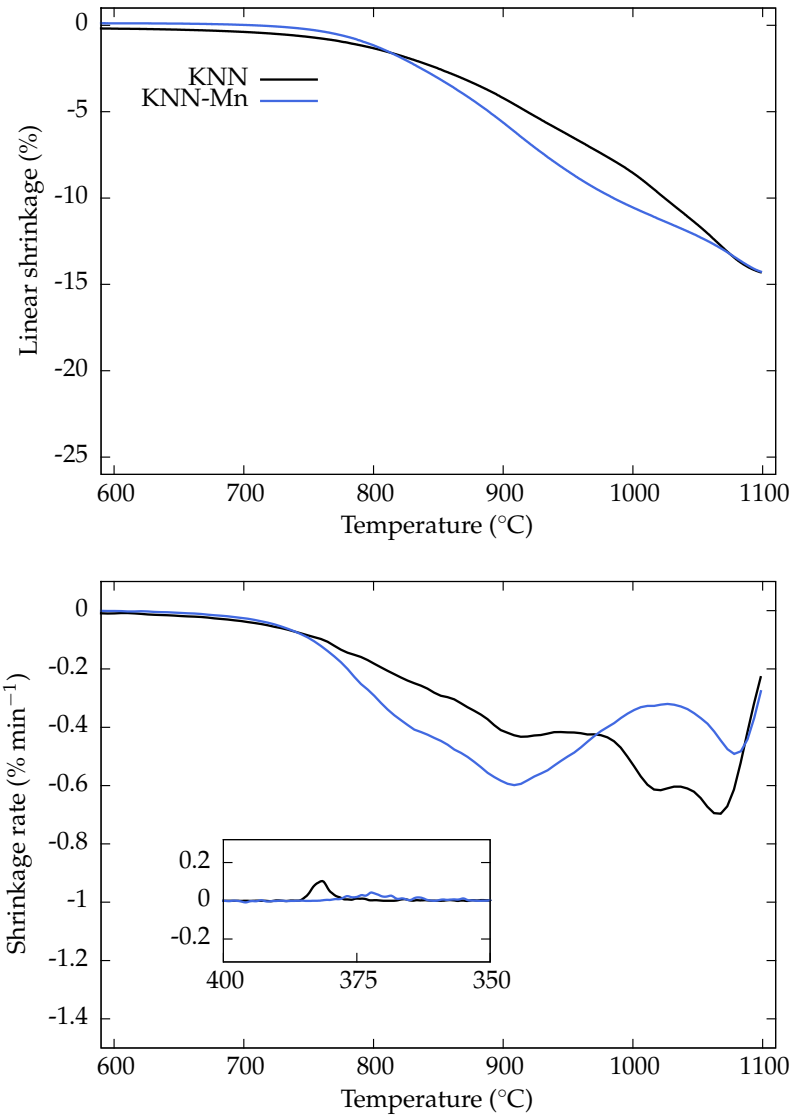

FIGURE 4.2: Dilatometer curves for the KNN powder, with and without addition of manganese oxide. Upper part: linear shrinkage, lower part: shrinkage rate. Inset plot shows shrinkage rate during cooling in the vicinity of the Curie point. Heating rate 10 °C min^{-1} in synthetic air atmosphere.

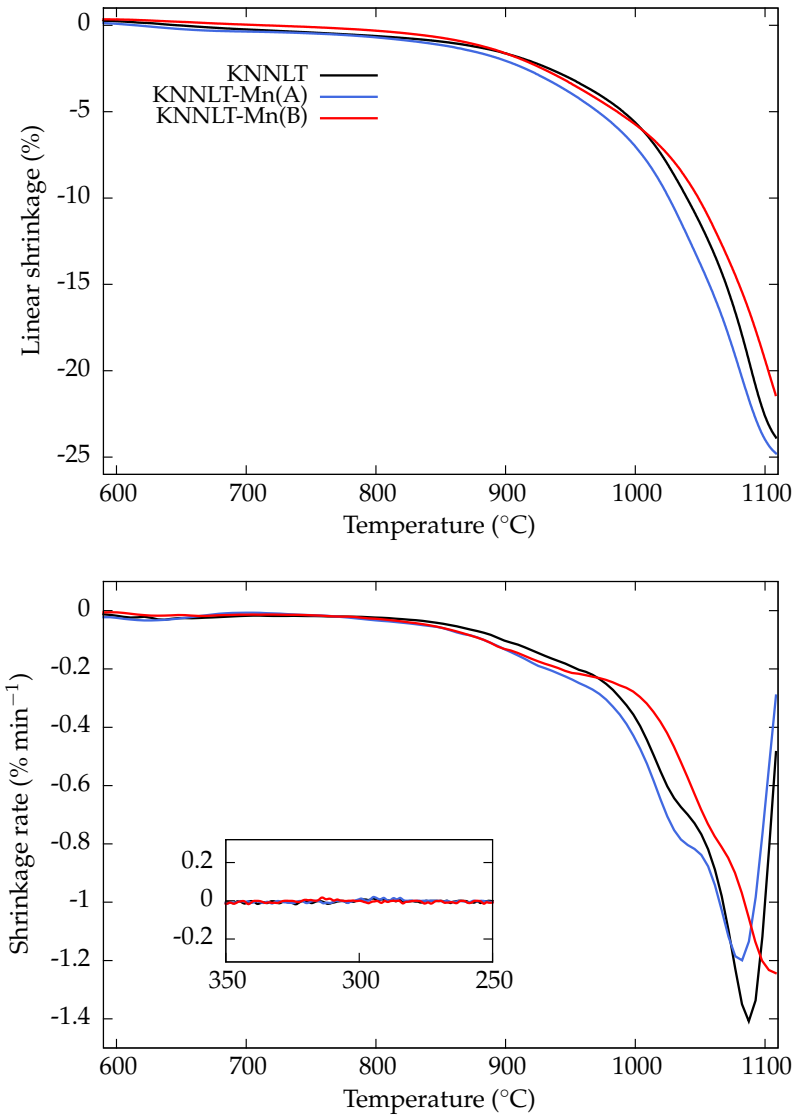

FIGURE 4.3: Dilatometer curves for the three KNNLT compositions considered. Upper part: linear shrinkage, lower part: shrinkage rate. Inset plot shows shrinkage rate during cooling in the vicinity of the Curie point. Heating rate 5 °C min^{-1} in synthetic air atmosphere.

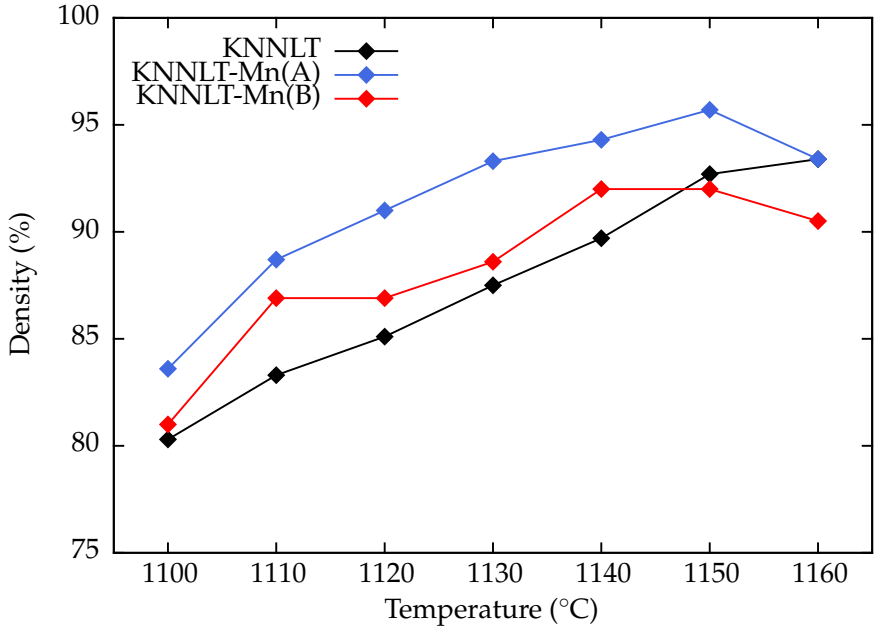

FIGURE 4.4: Relative density of isothermally sintered KNNLT samples, as measured by Archimedes' method and given relative to the theoretical value of 4.99 g cm^{-3}. Holding time was 1 hour in an atmosphere of air.

4.2 Microstructure and density of sintered samples

The density of the different samples is shown in Table 4.2 as percentage of theoretical density, along with the sintering conditions for each sample. Green body density was determined by geometrical measurements and is given for non-textured samples only. Most sintered samples reached more than 90 % of theoretical density, with the highest density obtained being 96.7 % for the KNNLT-Mn(A) sintered for 14 hours. The KNNLT-Mn(A) samples generally reach higher densities than KNN-Mn, despite having lower green densities.

Figure 4.5 shows micrographs of non-textured materials used for further characterization. Figures 4.6 and 4.7 show green tapes and sintered laminates, respectively, of the textured materials used for further characerization, with tape casting direction left–right in all images. Notably, the green KNN-Mn tape

TABLE 4.2: Density of samples studied in this work, along with composition and sintering conditions.

Sample	Hours sintered	Temperature (°C)	Density (%)	
			Green	Sintered
KNN-Mn	3	1100	59	92.0
KNN-Mn	14	1100	66	93.9
t-KNN-Mn	14	1130		89.2
KNNLT-Mn(A)	3	1150	46	95.0
KNNLT-Mn(A)	14	1150	44	96.7
t-KNNLT-Mn(A)	14	1150		91.2

in Figure 4.6(a) and (c) has a very uneven, crater-like surface topography, while the green KNNLT-Mn(A) tape in Figure 4.6(b) and (d) is comparatively smooth. The KNNLT-Mn(A) tape is also visibly textured, with template particles well aligned along the casting direction, while it is hard to say anything about the degree of texture in the KNN-Mn tape from the micrographs alone.

As can be seen in the backscattered electron (BSE) image in Figure 4.7(d), the t-KNNLT-Mn(A) sample has huge inclusions of a secondary phase. The secondary phase seems to be textured in the sense that the elongated inclusions are somewhat oriented along the tape casting direction. In comparison, the BSE image of t-KNN-Mn in Figure 4.7(c) shows no such phase contrast, indicating a phase pure material. There is also very little phase constrast to be seen in the BSE images of non-textured samples in Figures 4.5(c) and (d), indicating that secondary phase formation is a problem mainly for t-KNNLT-Mn(A).

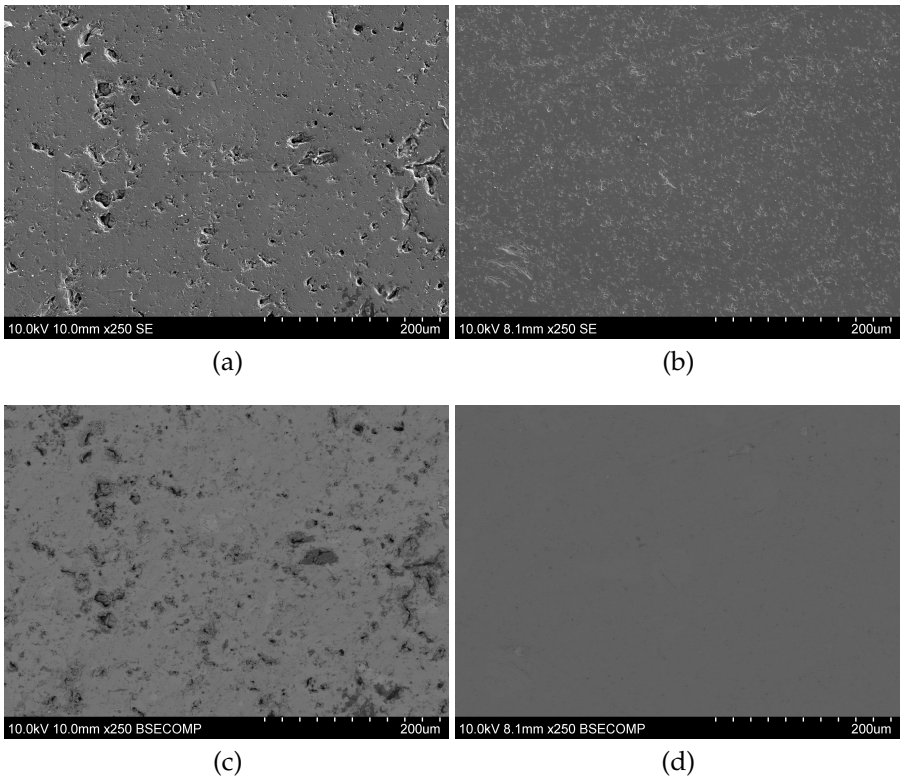

FIGURE 4.5: SEM micrographs of non-textured samples: (a) and (c) KNN-Mn; (b) and (d) KNNLT-Mn(A).

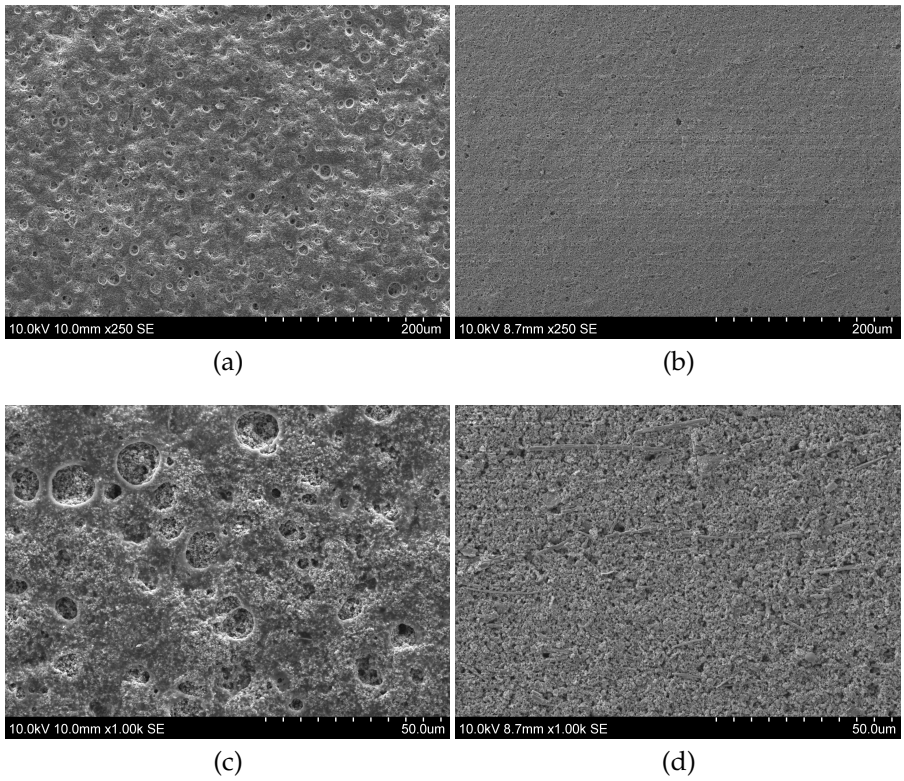

FIGURE 4.6: SEM micrographs of green tapes: (a) and (c) KNN-Mn; (b) and (d) KNNLT-Mn(A).

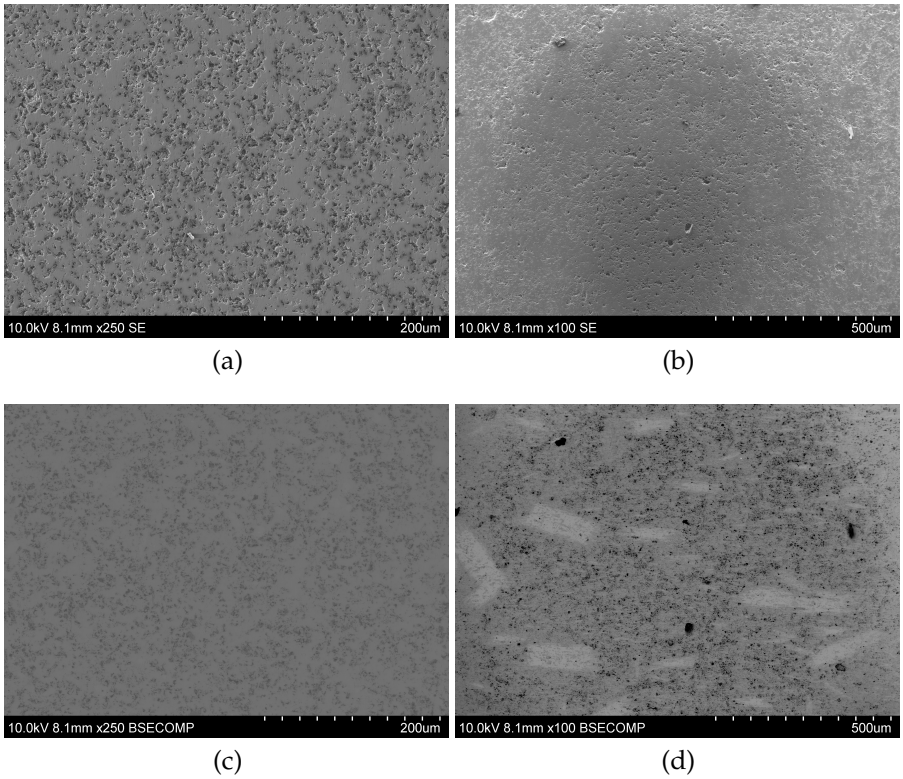

FIGURE 4.7: SEM micrographs of textured samples: (a) and (c) t-KNN-Mn; (b) and (d) t-KNNLT-Mn(A). Notice slightly different scale bar between the two samples.

4.3 Phase purity

X-ray diffractograms of all samples are displayed in Figures 4.8 and 4.9, for KNN-Mn and KNNLT-Mn(A) samples, respectively. While all samples show small amounts of secondary phase impurities, the t-KNNLT-Mn(A) sample stands out in possessing very distinct diffraction lines from a secondary phase in addition to the main perovskite phase. This fits well with the SEM micrograph in Figure 4.7(d), which shows secondary phase inclusions in t-KNNLT-Mn(A). The tetragonal tungsten bronze phase $K_3Li_2NbO_{15}$ (PDF card 00-052-0157) appears to be the closest match available for the secondary phase, although a few diffraction lines from this structure are missing in the experimental pattern. The tetragonal tungsten bronze phase $K_2Nb_4O_{11}$ (PDF card 00-031-1059) seems to be a possible match of the secondary phase visible in t-KNN-Mn #1 in Figure 4.8.

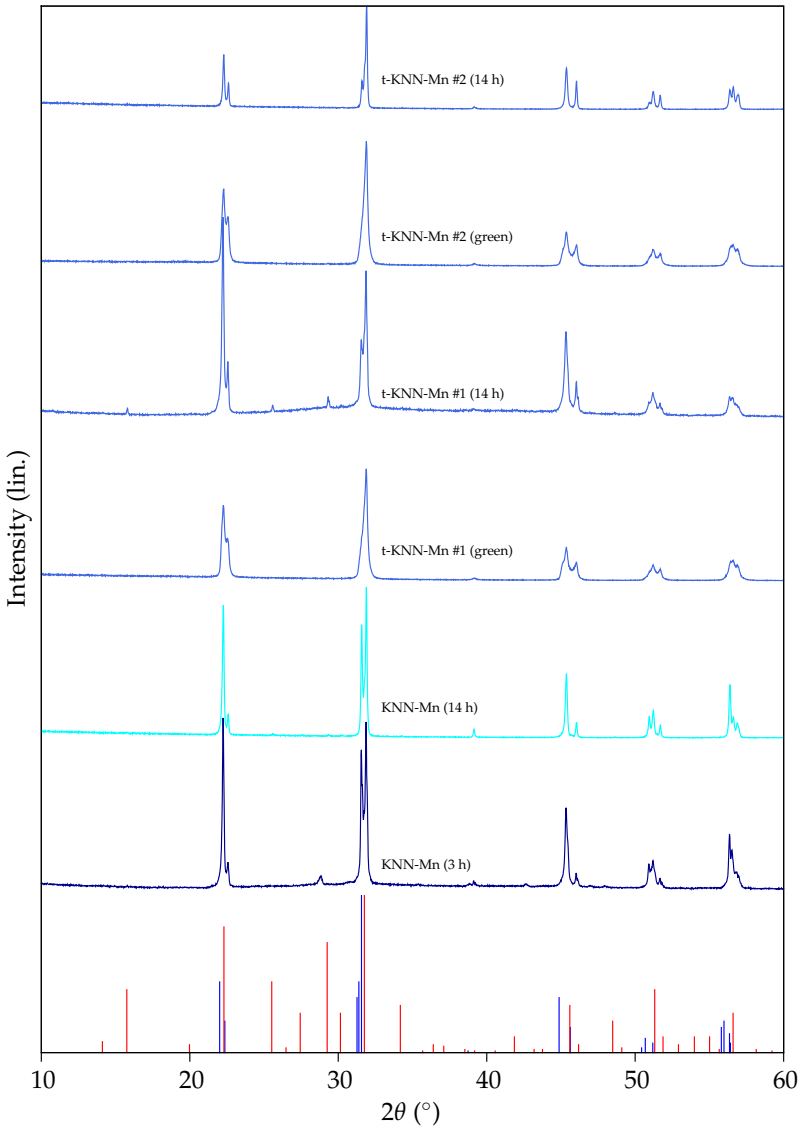

FIGURE 4.8: X-ray diffractograms of KNN-Mn samples. References at bottom are $KNbO_3$ (blue, PDF card 00-032-0822) and $K_2Nb_4O_{11}$ (red, PDF card 00-031-1059).

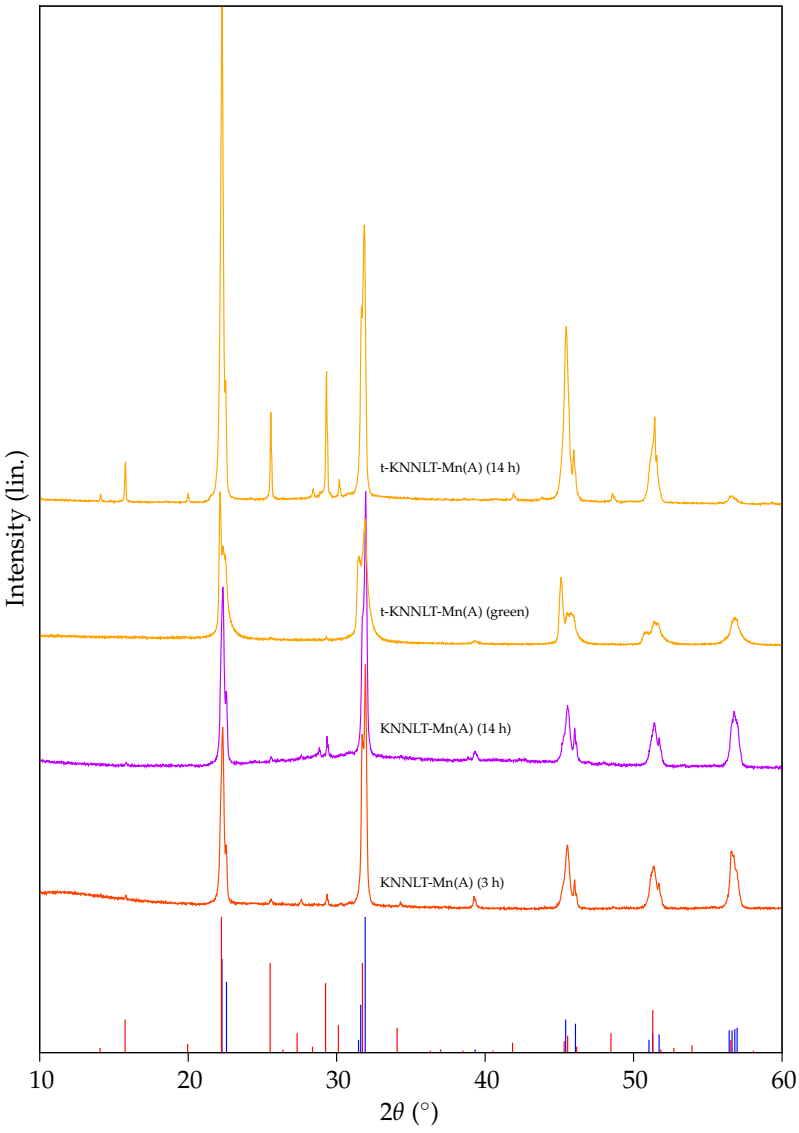

FIGURE 4.9: X-ray diffractograms of KNNLT-Mn(A) samples. References at bottom are $0.94K_{0.5}Na_{0.5}NbO_3$–$0.06LiTaO_3$ (blue, PDF card 00-060-0329) and $K_3Li_2Nb_5O_{15}$ (red, PDF card 00-052-0157).

4.4 Degree of texture

Calculated Lotgering factors are given in Table 4.3. For the textured KNNLT-Mn(A) sample, it was not possible to calculate the Lotgering factor, due to the substantial amounts of a secondary phase. An attempt was made to do a deconvolution of the patterns through Pawley fitting, but this did not succeed due to the overlap between diffraction lines from the perovskite and the secondary phase, and the fact that an exact match to the secondary phase diffraction lines could not be found.

TABLE 4.3: Calculated Lotgering factors for textured samples, both green tapes and sintered laminates.

Textured sample	Non-textured reference	Lotgering factor f (%)
t-KNN-Mn (green)	KNN-Mn (14 h)	5
t-KNN-Mn (14 h)	KNN-Mn (14 h)	21
t-KNNLT-Mn(A) (green)	KNNLT-Mn(A) (14 h)	22
t-KNNLT-Mn(A) (14 h)	KNNLT-Mn(A) (14 h)	–

4.5 Piezoelectric and dielectric properties

Hysteretic behaviour

Hysteresis curves of strain, polarization and current vs. electric field are shown in Figures 4.10, 4.11 and 4.12, respectively.

The strain hysteresis curves show that the non-textured KNNLT-Mn(A) samples achieve the highest strain of all samples, although the strain response is not completely symmetrical with respect to polarity of the eletric field. Nevertheless, they reach higher strains than both the textured and the non-textured KNN-Mn samples, which again outperform the textured KNNLT-Mn(A).

The polarization curves in Figure 4.11 are all similar in shape, with the exception of non-textured KNN-Mn (3 h). The loop for non-textured KNN-Mn (3 h) is wider and more open in shape than the rest, with higher values of both remanent polarization and coercive field. It is also more rounded at the wedges than the others, which is a sign of possible leakage current. This is also supported by the high value of remanent polarization. The two non-textured KNNLT-Mn(A) samples have very similar polarization curves,

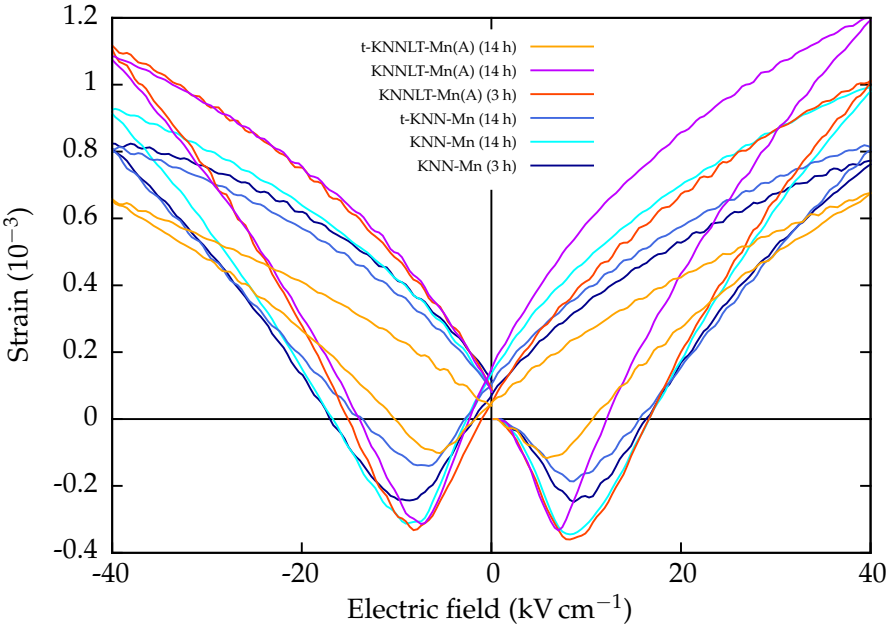

FIGURE 4.10: Strain hysteresis loops for the samples investigated, acquired at 40 kV cm^{-1} and 0.25 Hz.

differing slightly only in the slope of the curves near the coercive field, while the textured KNNLT-Mn(A) is more similar to the textured KNN-Mn.

The trends observed in the polarization curves are in certain aspects even more visible in the plot of current vs. electric field, Figure 4.12, which in reality is the derivative of the polarization loops in Figure 4.11. For example, it is easily seen that the non-textured KNNLT-Mn(A) sample sintered for 14 hours has the sharpest and highest current peak near the coercive field, corresponding to this sample also having the steepest polarization curve at this point and thus the most pronounced switching behaviour. It can also be seen that at electric fields well above the coercive field, the non-textured KNN-Mn sample has a higher current than all other samples, which corresponds to this sample having a higher ohmic current or leakage current.

All data on hysteretic behaviour presented in Figures 4.10, 4.11 and 4.12 was aquired at an electric field amplitude of 40 kV cm^{-1}. Data for lower amplitudes

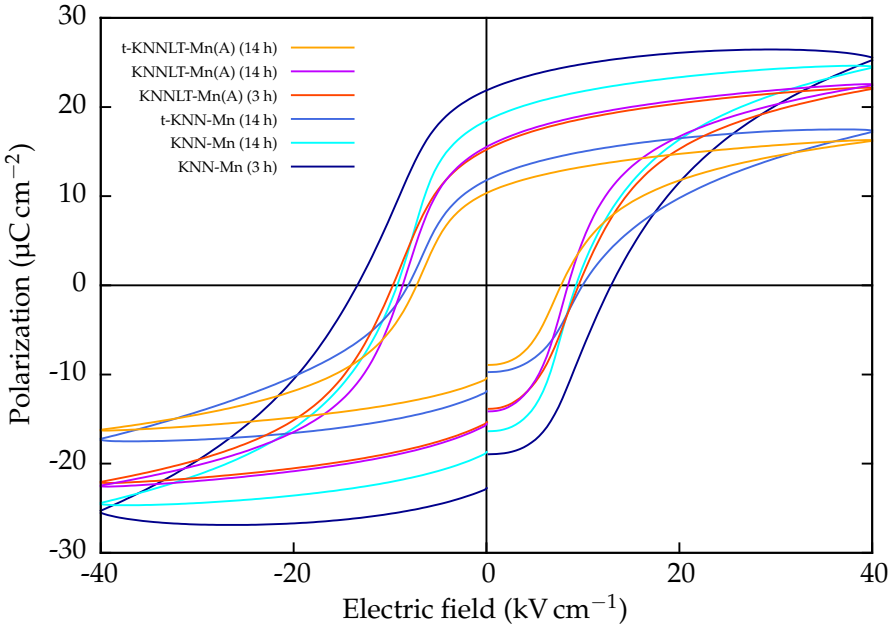

FIGURE 4.11: Polarization hysteresis loops for the samples investigated, acquired at 40 kV cm^{-1} and 0.25 Hz.

is collected in Appendix C.

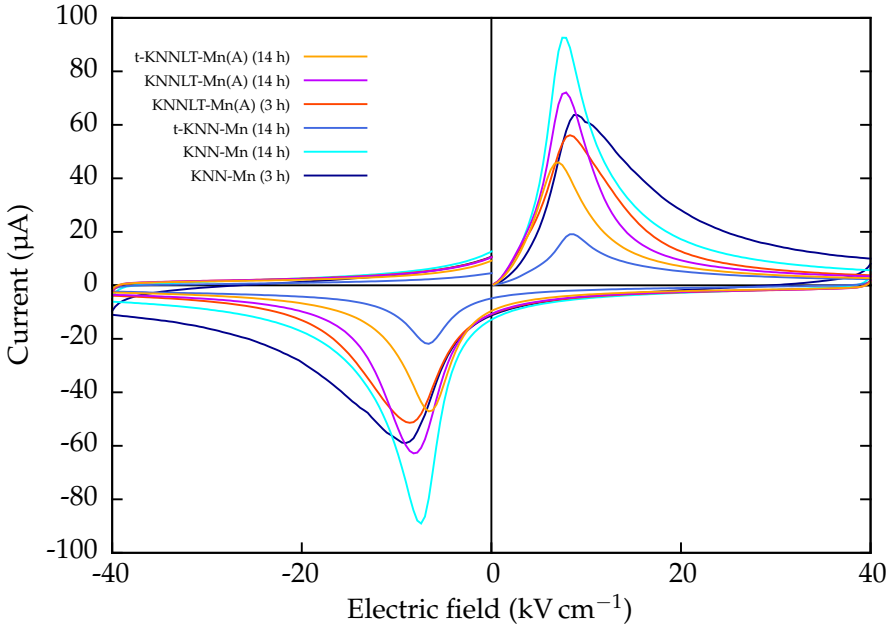

FIGURE 4.12: Current hysteresis loops for the samples investigated, acquired at 40 kV cm^{-1} and 0.25 Hz.

Converse piezoelectric coefficient

The converse piezoelectric coefficient d_{33av} is determined by a the average slope of unipolar strain–electric field curves; a higher value of d_{33av} means that a higher strain is obtained under application of a certain electric field. Figure 4.13 shows strain–electric field curves for unipolar fields with an amplitude of 40 kV cm^{-1}, while additional curves for other amplitudes can be found in Appendix C.

Figure 4.14 shows the development of the converse piezoelectric coefficient d_{33av} in response to varying electric fields. In general, this plot confirms what can be assumed from the strain loops in Figures 4.10 and 4.13. Again it can be seen that the non-textured KNNLT-Mn(A) is the best of the samples, with the one sintered for 14 hours reaching a maximum d_{33av} value of 259 pm V^{-1}. The textured KNNLT-Mn(A) performs similarly to the KNN-Mn samples, both the

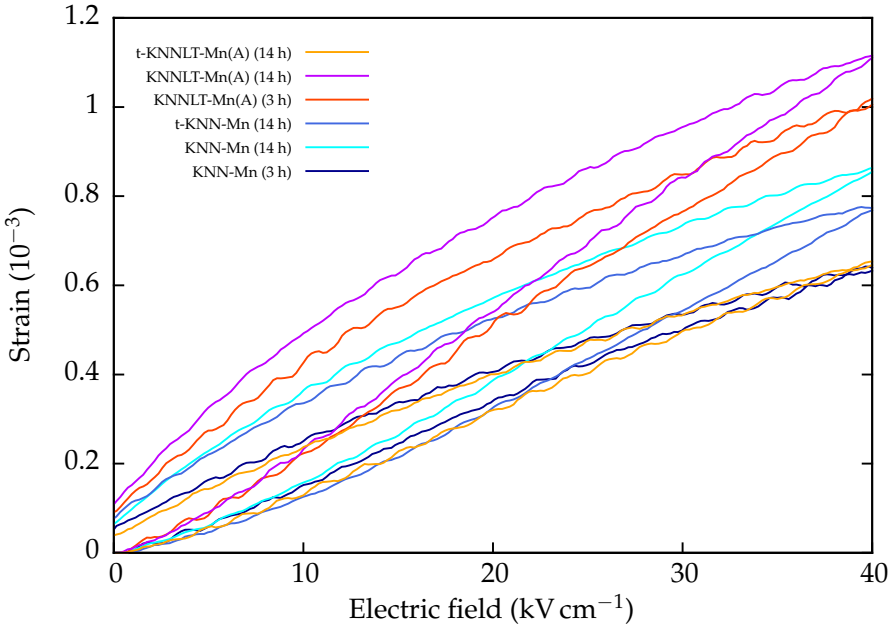

FIGURE 4.13: Plot of strain versus electric field for the different samples investigated. The average slope of the curve determines the piezoelectric coefficient d_{33av}. Measurements done with a frequency of 0.25 Hz and an amplitude of 40 kV cm^{-1}.

textured and non-textured ones, which again are not very different from one another, reaching d_{33av} values of 150 pm V^{-1} to 200 pm V^{-1} at high fields.

The effect of poling is included as dashed lines in Figure 4.14. Generally, poling causes a vertical shift in the piezoelectric response curves, while the shape of the curves remains relatively unchanged.

Temperature dependence of piezoelectric properties

The converse piezoelectric coefficient d_{33av} of KNNLT-Mn(A) (3 h) is plotted versus temperature in Figure 4.15. As usual, the highest electric field yields the highest piezoelectric coefficient. In addition, there is a broad peak in the piezoelectric coefficient at around 60 °C, which is much more pronounced on cooling the sample than on heating.

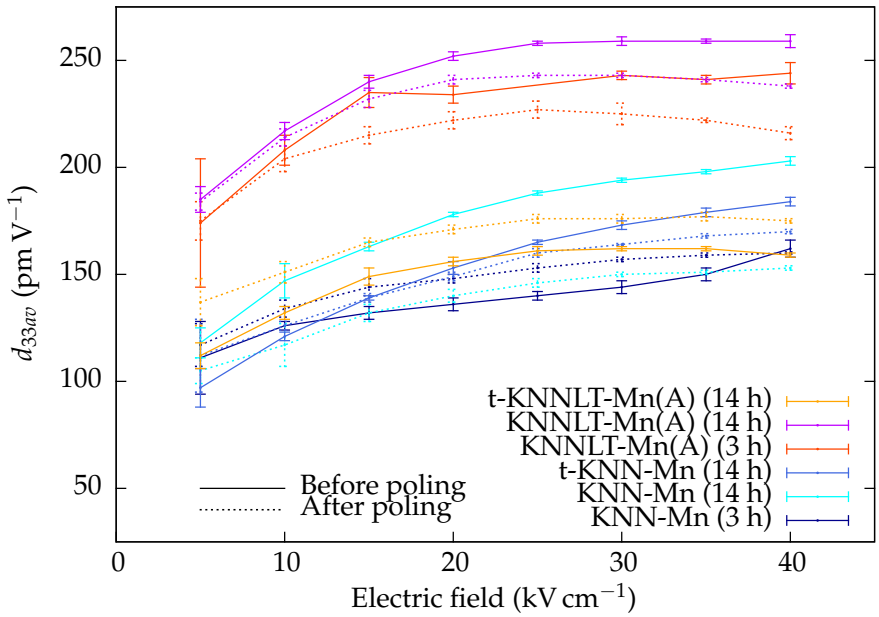

FIGURE 4.14: Dependence of the converse piezoelectric coefficient, d_{33av}, on electric field strengths for the samples investigated. Each point is the average of 10–15 measurements, with the error bars corresponding to the $n - 1$ standard deviation. Dashed lines denote measurements after poling samples at 20 kV cm^{-1} while cooling from 100 °C to room temperature. All measurements done at 0.25 Hz.

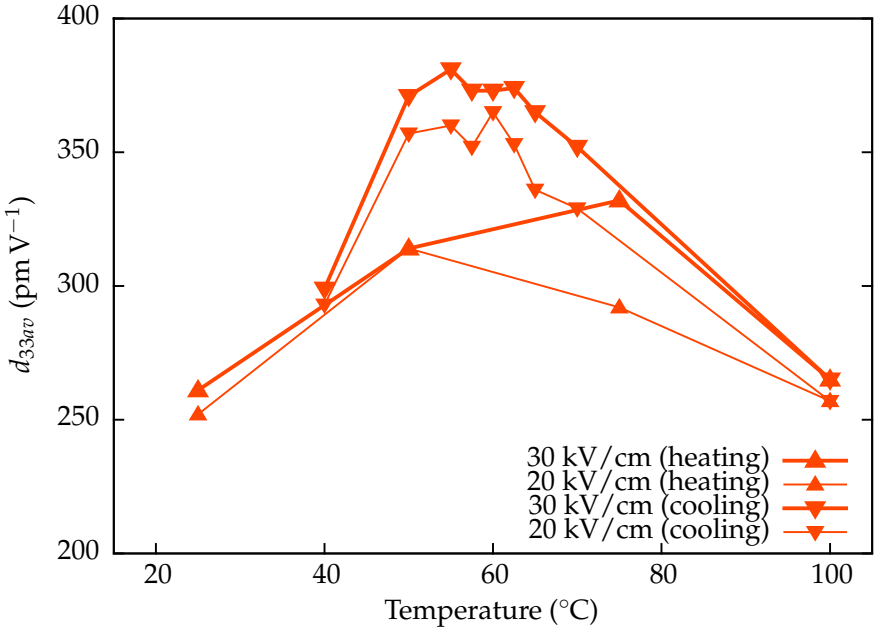

FIGURE 4.15: Temperature dependence of the converse piezoelectric coefficient d_{33av} for non-textured KNNLT-Mn(A) sintered for 3 hours. Measurements were done at electric field amplitudes of 30 kV cm^{-1} (thick line) and 20 kV cm^{-1} (thin line) and a frequency of 0.25 Hz.

Impedance spectroscopy

Plots of relative permittivity and dielectric loss versus temperature at different frequencies are given in Figure 4.16 for KNN-Mn (3 h) and Figure 4.17 for KNNLT-Mn(A) (3 h), both measured by continuous heating at $2\,^{\circ}\mathrm{C\,min^{-1}}$. Relative permittivity is shown for frequencies from 1 Hz to 1 MHz, while dielectric losses are shown for frequencies from 100 Hz to 1 MHz.

The O–T transition temperature, $T_{\mathrm{O-T}}$, is taken as the steepest point of the permittivity curves, determined by the derivative curves given as insets in the plots. Figure 4.18 shows the same type of data for KNNLT-Mn(A) (3 h) in the range 20 °C to 100 °C, but measured by heating in steps and stabilizing at each temperature before measuring at the different frequencies. The permittivity data in this stepwise scan is similar to the corresponding region of the continuous scan in Figure 4.17, although the dielectric losses are lower in the stepwise scan.

A Curie–Weiss plot, showing reciprocal relative permittivity versus temperature, is given for KNNLT-Mn(A) in Figure 4.19, using the same data as in Figure 4.17. The Curie–Weiss temperature θ is determined by a linear fit of the 1 MHz curve in the range 350 °C to 400 °C, in accordance with the Curie–Weiss law, Equation (3.6).

Experimental values of characteristic temperatures for both materials are summarized in Table 4.4.

TABLE 4.4: Summary of characteristic temperatures (°C) as measured by dielectric spectroscopy of samples sintered for 3 hours.

	$T_{\mathrm{O-T}}$	T_{C}	θ
KNN-Mn	170	–	–
KNNLT-Mn(A)	49	319	302

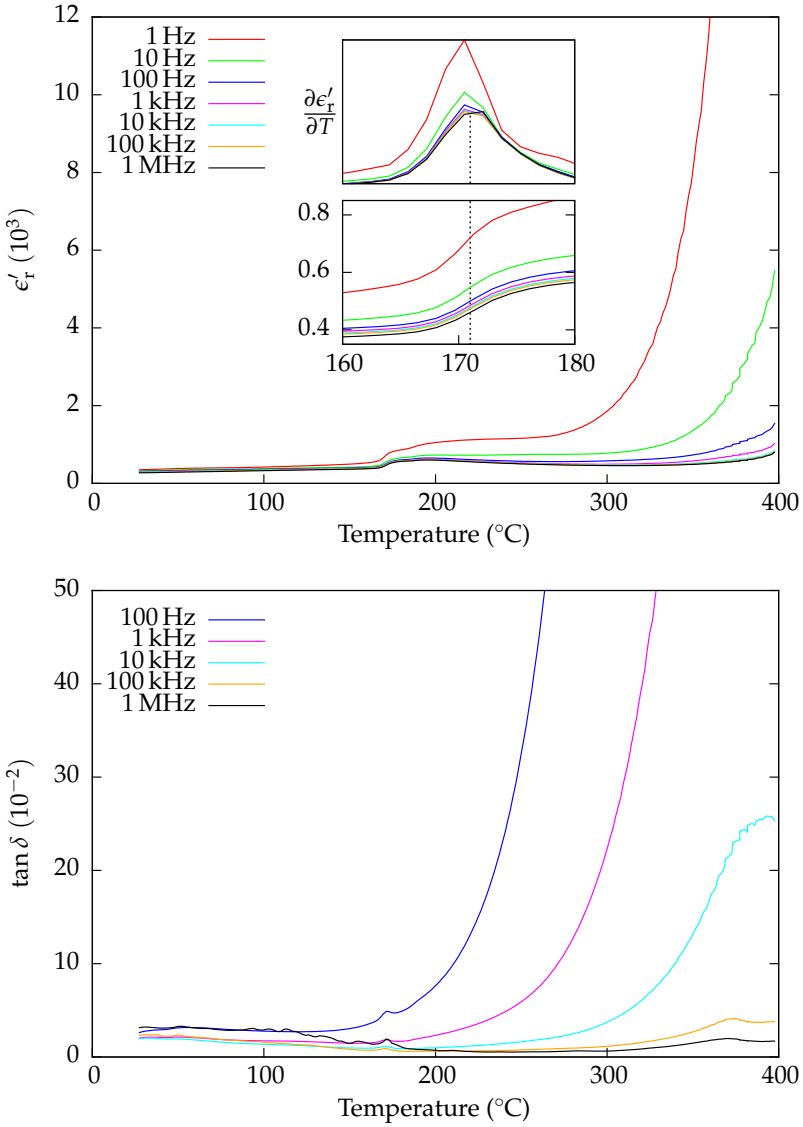

FIGURE 4.16: Dielectric properties of KNN-Mn (3 h) as function of temperature for different frequencies. Bottom inset: magnification of area around the O–T transition; upper inset: derivative of curves in bottom inset. T_{O-T} is taken as the steepest point of the 1 MHz curve at 171 °C (dotted line).

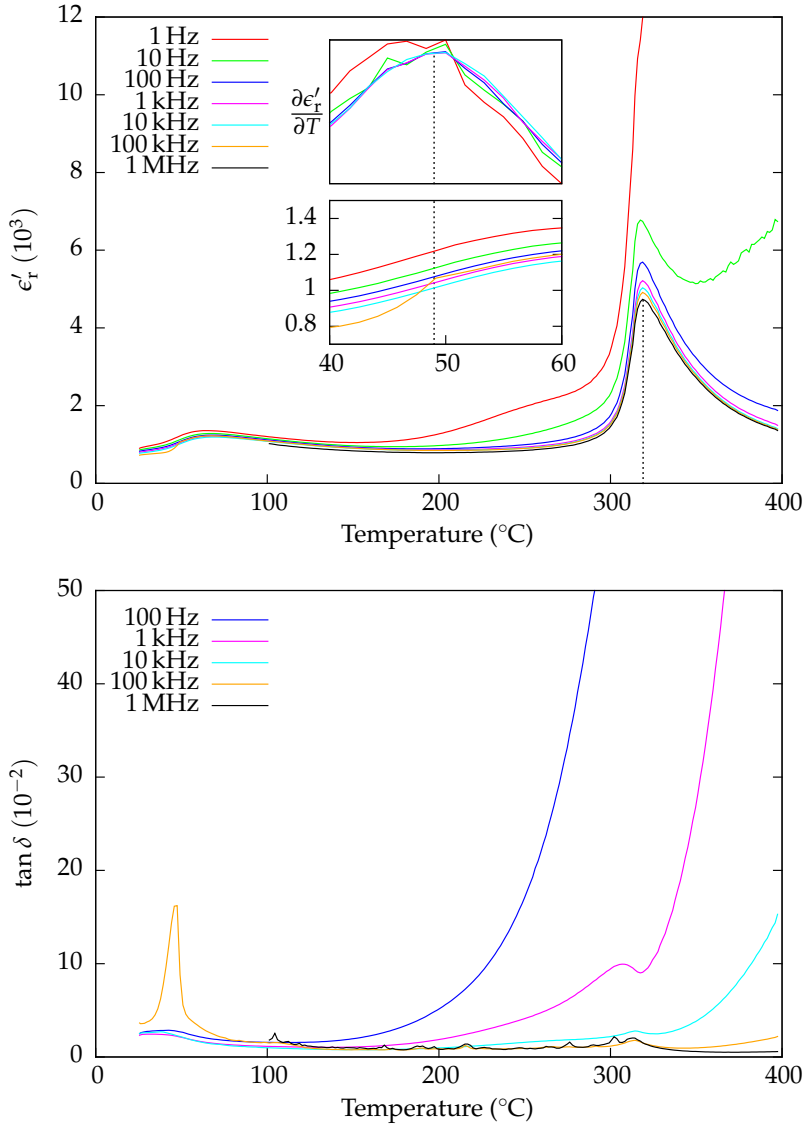

FIGURE 4.17: Dielectric properties of KNNLT-Mn(A) (3 h) as function of temperature for different frequencies (1 MHz not shown below 100 °C due to unstable behaviour in this range). Bottom inset: magnification of area around the O–T transition; top inset: derivative of curves in bottom inset. T_{O-T} is taken as the steepest point of the 10 kHz curve at 49 °C, while T_c is taken as the maximum of the 1 MHz curve at 319 °C (dotted lines).

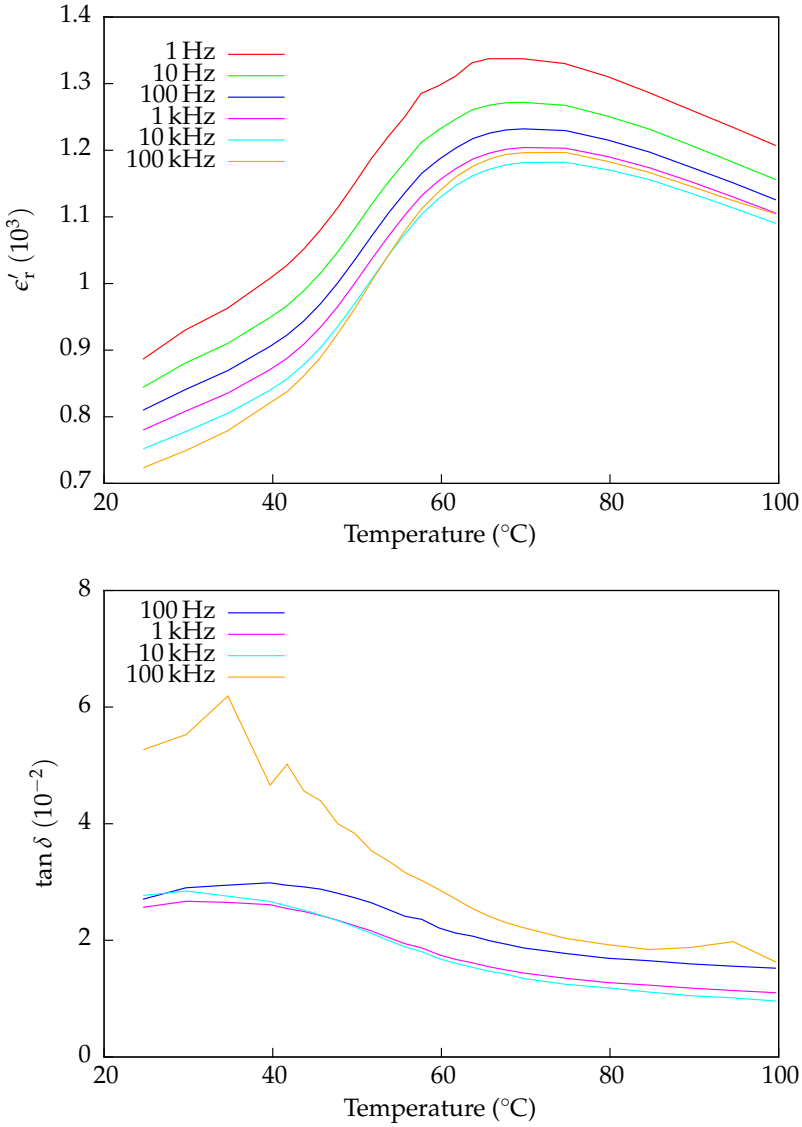

FIGURE 4.18: Dielectric properties of KNNLT-Mn(A) (3 h) as function of temperature, measured by heating in steps and stabilizing at each temperature before doing sweeps at the different frequencies.

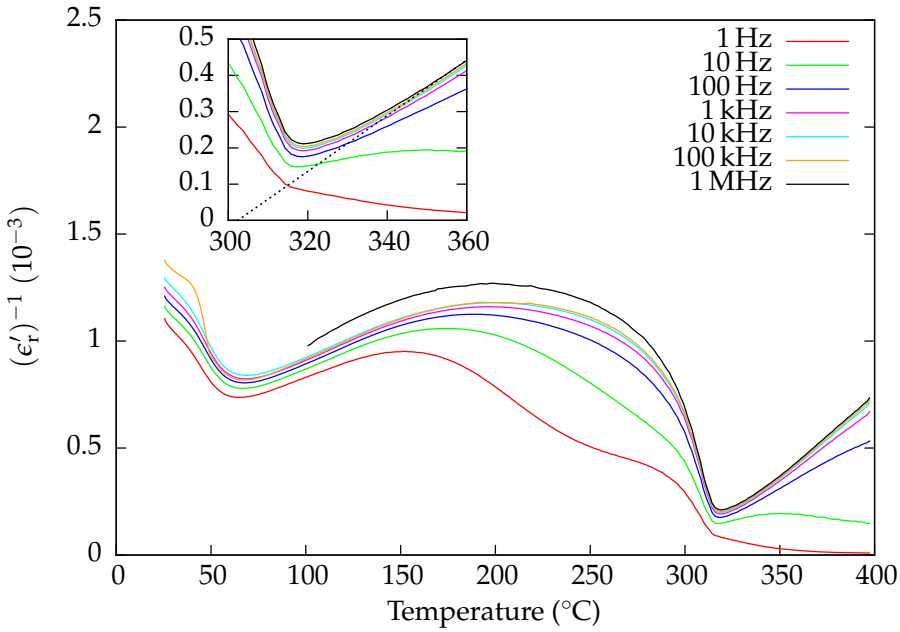

FIGURE 4.19: Curie–Weiss plot (reciprocal relative permittivity versus temperature) for KNNLT-Mn(A) (3 h) at different frequencies (1 MHz not shown below 100 °C due to unstable behaviour in this range). Inset: magnification of area around Curie point. Dotted line shows linear fit (Curie–Weiss law) based on 1 MHz curve, intersecting at 302 °C.

Chapter 5

Discussion

5.1 Effect of material composition

Comparability of the materials

As stated in Table 3.1, the KNN-Mn material has the composition $K_{0.5}Na_{0.5}NbO_3$, with 0.5 mol% Mn^{2+} added, while the KNNLT-Mn(A) has the composition $((K_{0.46}Na_{0.54})_{0.97}Li_{0.03})_{0.995}Mn_{0.005}Nb_{0.81}Ta_{0.19}O_3$, where Mn is added specifically to the A site in the perovskite lattice. Hence, there are two important differences between the two materials, in addition to the Li- and Ta-doping: first, the K/Na ratio is different, being 50/50 in KNN-Mn and 46/54 in KNNLT-Mn(A) (and in the other KNNLT compositions that were initially considered); second, there is the difference between adding Mn and substituting Mn into the lattice.

Upon addition of Mn^{2+} to a perovskite $[A^+][B^{5+}]O_3$, the following defect reactions are in principle possible, depending on which lattice site the manganese ions prefer:

$$5\,\mathrm{MnO} \xrightleftharpoons{\mathrm{ABO_3}} 5\,\mathrm{Mn}_\mathrm{A}^{\bullet} + 5\,\mathrm{O}_\mathrm{O}^{\times +}\mathrm{v}_\mathrm{B}^{''''''} \tag{5.1}$$

$$2\,\mathrm{MnO} \xrightleftharpoons{\mathrm{ABO_3}} 2\,\mathrm{Mn}_\mathrm{A}^{\bullet} + \mathrm{O}_\mathrm{O}^{\times +}\mathrm{O}_\mathrm{i}^{''} \tag{5.2}$$

if the manganese ions go to the A site, or

$$2\,\mathrm{MnO} \xrightleftharpoons{\mathrm{ABO_3}} 2\,\mathrm{Mn}_\mathrm{B}^{'''} + 2\,\mathrm{O}_\mathrm{O}^{\times +}3\,\mathrm{v}_\mathrm{O}^{\bullet\bullet} \tag{5.3}$$

$$5\,\mathrm{MnO} \xrightleftharpoons{\mathrm{ABO_3}} 5\,\mathrm{Mn}_\mathrm{B}^{'''} + 5\,\mathrm{O}_\mathrm{O}^{\times +}3\,\mathrm{B}_\mathrm{i}^{\bullet\bullet\bullet\bullet\bullet} \tag{5.4}$$

if the manganese ions go the B site. While it is far from certain that manganese still is in the 2+ oxidation state after calcination and sintering, the ionic compensation mechanisms would be similar if the oxidation state was, for example, 4+. For ions preferring the A site, the cation vacancy mechanism in Equation (5.1) is by far the most plausible, since few crystal structures actually have enough space in the lattice to accomodate the relatively large interstital oxygen ions as in Equation (5.2). For the same reason, the oxygen vacancy mechanism in Equation (5.3) is much more plausible than the interstitial cation mechanism in Equation (5.4) for a crystal structure that is as closely packed as the perovskite structure.

The mechanisms discussed above are not only relevant for the properties of the KNN-Mn material, but also for the KNNLT-Mn(A) and KNNLT-Mn(B) materials, and the differences between these two. If manganese strongly prefers one site over another, it will not be possible to synthesize both varieties of Mn-doped KNNLT, at least not in phase-pure form. If, for instance, Mn prefers the A site, the KNNLT-Mn(B) composition will be unstable, with Mn diffusing from B-sites to A-sites. This would lead to an A-site charge excess, which would be compensated by cation vacancies similar to in Equation (5.1). If, on the other hand, Mn strongly prefers the B site, KNNLT-Mn(A) will be unstable, and Mn will diffuse from A-sites to B-sites, leading to a B-site charge excess. The mechanism that is most likely to compensate for this is formation of oxygen vacancies similar to Equation (5.3).

It is not known which of the compositions KNNLT-Mn(A) or KNNLT-Mn(B) is inherently more stable, or whether both might be stable due to little site preference for the Mn ions. However, based on the above considerations, it can be inferred that if the KNNLT-Mn(A) is less stable, the result is probably formation of oxygen vacancies, while if the KNNLT-Mn(B) is less stable, the result is likely to be the formation of B-site cation vacancies. Kizaki et al.[38] argumented that doping of KNN with Mn most likely results in Mn^{2+} at the B-sites, based on the fact that the lattice parameters of KNN single crystals increased with increasing dopant level, which can be explained by Mn^{2+} being larger than Nb^{5+}. However, they also found that the average valence state of Mn increased through annealing the crystals at 1100 °C in air, indicated by an increased signal from Mn^{4+} measured by electron spin resonance spectroscopy. The average valence state of Mn is therefore likely to be higher than 2+ in the KNN-Mn and KNNLT-Mn(A) compositions as well.

Effect of doping with manganese

While a comparative study was not done here between materials with and without Mn additions, it is generally accepted that the addition of Mn in the form of MnO_2 has an effect in reduction of leakage current and lowering of dielectric losses.[4,10] The two are connected, since the presence of an ohmic leakage current in a dielectric will contribute to a current component in phase with the applied alternating voltage, thereby causing energy dissipation. The mechanism by which Mn reduces leakage current in dielectrics is generally thought to be the reactions

$$Mn^{4+} + e' \longrightarrow Mn^{3+} \tag{5.5}$$

and

$$Mn^{3+} + e' \longrightarrow Mn^{2+}, \tag{5.6}$$

which decrease electric conductivity by trapping electrons.

A study by Lin et al.[39] on KNN single crystals addition-doped with Mn, concluded with an increase in relative permittivity from 240 to 730 for crystals doped with 0.5 % MnO_2 as compared to pure KNN crystals, while the direct piezoelectric coefficient d_{33} increased from 160 pC N^{-1} to 270 pC N^{-1}. This was explained by a decrease in average domain width from 25 µm to 9 µm, with the higher domain wall density leading to increased piezoelectric and dielectric properties.

From the dilatometry data (Figure 4.3) and isothermal sintering data (Figure 4.4) it can safely be concluded that KNNLT-Mn(A) sinters better than KNNLT, while KNNLT-Mn(B) does not improve that much on the pure material. While Mn is usually not used primarily as a sintering aid in KNN-based materials, the author has previously discussed[6] how addition of Mn to KNN improves sintering. The improved densification is thought to be due to formation of oxygen vacancies according to Equation (5.3), which could influence the mobility of both oxygen ions and cations in the material. As was mentioned above, the same thing can be expected to happen with KNNLT-Mn(A), especially if the manganese ions prefer the B sites of the perovskite structure instead of the A sites they are nominally added to. In KNNLT-Mn(B) the manganese ions are already at their preferred lattice sites, and thus do not contribute to formation of oxygen vacancies to the same extent.

Piezoelectric properties

From the plot of d_{33av} versus electric field in Figure 4.14, it can be seen that the KNNLT-Mn(A) performs better than KNN-Mn on a general basis. The exception is t-KNNLT-Mn(A), which performs similarly to KNN-Mn, almost certainly due to the formation of a secondary phase. This trend is naturally reflected in the unipolar strain loops in Figure 4.13, on which the d_{33av} is based, and also to some extent in the bipolar strain loops in Figure 4.10.

The dependence of converse piezoelectric coefficient on electric field strength (Figure 4.14) is slightly different for the two material compositions. While the KNNLT-Mn(A) samples generally reach saturation around $25\,\mathrm{kV\,cm^{-1}}$, and in certain cases even decrease in d_{33av} for higher field strengths, the KNN-Mn materials increase steadily all the way up to $40\,\mathrm{kV\,cm^{-1}}$. This phenomenon can be explained by a difference in coercive field for the two compositions, with KNNLT-Mn(A) having a lower coercive field than KNN-Mn. This can be seen from the strain hysteresis loops in Figure 4.10, where the coercive field corresponds to the minimum on the curves. There is a notable difference between for example the KNNLT-Mn(A) (14 h) curve and the KNN-Mn (14 h) curve, although both materials have coercive fields between $5\,\mathrm{kV\,cm^{-1}}$ and $10\,\mathrm{kV\,cm^{-1}}$. A lower coercive field means that domain switching occurs at a lower electric field strength, so that polarization saturation is reached sooner. For the non-textured samples sintered for 3 hours, the difference is less pronounced.

This difference between coercive field for the two compositions should in principle also be visible from the polarization hysteresis loops in Figure 4.11, although here the difference is not so clearly seen. A partial explanation of this is that the polarization loops are also affected by leakage current, which is easily seen on the KNN-Mn (3 h) sample. The piezoelectric testing device does not distinguish between ohmic current and displacement current, so ohmic leakage current will falsely contribute to detected polarization. Leakage current is, however, easily identified as such from the current hysteresis loops in Figure 4.12, where it can be seen that the KNN-Mn (3 h) sample has a significant current at electric fields well away from the coercive field, which is an indication of ohmic current.

Phase transitions

In KNN-based materials, including KNNLT materials, there are two phase transitions to consider in the temperature range from room temperature and

upwards: the orthorhombic–tetragonal transition, which happens anywhere from near room temperature in certain KNNLT compositions, and up to around 200 °C in pure KNN; and the tetragonal–cubic transition, or Curie point, which happens at around 400 °C in pure KNN and at lower temperature in most KNNLT compositions.

Several of the characterization techniques utilized in this work can be used to extract information about phase transitions, specifically dilatometry, dielectric spectroscopy and piezoelectric characterization. However, as the phase transitions in KNN-Mn happen at higher temperatures than in KNNLT-Mn(A), not all transitions are possible to study with all techniques.

The dilatometer curves in Figure 4.2 show that the Curie transition, which happens at around 380 °C when cooling the pure KNN, is shifted around 10 °C lower upon addition of 0.5 mol% manganese oxide. This shift is consistent with a study by Lin et al.,[39] who reported that the O–T and Curie transition temperatures of KNN-Mn single crystals, with composition identical to that in this work, decreased by 15 °C and 7 °C, respectively. The transition temperatures were different, however, with the O–T and Curie transitions happening at 193 °C and 416 °C, respectively. There are at least two possible reasons for this difference: firstly, the value of 416 °C by Lin et al.[39] was measured by dielectric spectroscopy, which is likely to be more accurate than dilatometry for this purpose. Secondly, the dielectric spectroscopy was done while heating the sample, while the dilatometer curves from this work mentioned above are from the cooling segment of the temperature program, making a certain temperature hysteresis possible.

The use of dielectric spectroscopy for determination of phase transition temperatures is a precise method, but still depends on a concise way of determining where the phase transitions happen. For the Curie transition of KNNLT-Mn(A) (Figure 4.17), this is quite obvious, with a very clear maximum of the permittivity curve at 319 °C. For the O–T transition of the same sample, however, the situation is not as clear. A maximum can be observed around 70 °C (also visible in Figure 4.18), but it is a very broad maximum, making it hard to point out an exact phase transition temperature. For the O–T transition of KNN-Mn (Figure 4.16) the maximum is even shallower. In both materials, however, the permittivity curves show a clearly marked *onset* of the O–T transition, with readily observed maxima in the derivative of permittivity with respect to temperature (inset plots in Figures 4.16 and 4.17). The point of maximum slope on the permittivity curves was therefore chosen as the point for comparing the O–T transition temperature between the KNN-Mn and KNNLT-Mn(A) compositions. This yields an O–T transition temperature that

is 121 °C lower in KNNLT-Mn(A) than in KNN-Mn.

Finally, the measurements of the converse piezoelectric coefficient d_{33av} at different temperatures (Figure 4.15) make it possible to observe the O–T transition in KNNLT-Mn(A) as the location of maximum piezoelectric response. The maxima of the cooling curves in Figure 4.15 occur at 55 °C (30 kV cm^{-1}) and 60 °C (20 kV cm^{-1}), which are both reasonably close to the value of 49 °C as determined by dielectric spectroscopy. It should be noted that this is a technique that is highly susceptible to noise in the measurements, making the location of the maximum uncertain. Nevertheless, the results from the piezoelectric measurements correspond well to the results obtained by Morozov et al.,[40] who studied a composition identical to KNNLT-Mn(B) in the same way. They reported a broad peak in converse piezoelectric coefficient in the same temperature range as here (50 °C to 70 °C), with a significant temperature hysteresis. They also found that the peak was sharper for phase pure materials synthesized by a precursor method, as compared to a conventional solid state reaction that gave less phase pure materials. The broadness of the peak could therefore be taken as a sign of phase impurity. It should be noted that with respect to piezoelectric applications that operate over a certain temperature range, a broad peak in performance could actually be beneficial, although phase purity is naturally wanted from a materials processing point of view.

5.2 Effect of texturing

Texture, density and phase purity

The overall goal of texturing is to increase the piezoelectric properties of the material. If, however, a crystallographic texture at the same time leads to unwanted side effects that destroy the piezoelectric properties, the justification for introducing texture vanishes. This should be the primary question when discussing the possible benefits of texturing KNN-based materials.

As was shown in Figure 4.14, there is a certain increase in the value of d_{33av} between KNN-Mn (3 h) and t-KNN-Mn (14 h) when comparing the unpoled samples. This difference can not simply be an effect of density, as the non-textured sample that was sintered for 3 hours obtained a density of 92.0 %, while the textured sample only obtained 89.2 % (Table 4.2). The KNN-Mn (14 h), however, has even higher values of d_{33av}, while also having the highest density of the KNN-Mn samples (93.9 %), suggesting that density plays a role, but without the connection being completely straightforward.

Poling seems to bring all the samples much closer together in terms of d_{33av}, making the difference between the three KNN-Mn samples comparatively small. There is, however, a possibility that this can be partly attributed to random scattering in the data between measurements on different samples. In addition, poling should not be expected to influence the converse piezoelectric coefficient as much as it would have influenced the direct piezoelectric coefficient, since the measurement of converse piezoelectric coefficient already takes place in relatively strong electric fields (in this case up to $40\,\mathrm{kV\,cm^{-1}}$, double the strength of the poling field).

Looking to the KNNLT-Mn(A) samples in Figure 4.14, the same tendency can be seen between the non-textured samples, in that the sample with the highest density also has the highest piezoelectric coefficient. Here, poling does not bring the samples closer to each other in terms of piezoelectric performance, but instead shifts both materials towards slightly lower d_{33av} values. Again, the possibility of data scattering between measurements on different samples should be kept in mind.

For KNNLT-Mn(A) there is unfortunately a lack of reliable data for the textured material, due to the large amount of a secondary phase formed during sintering. The assumption that the secondary phase forms during sintering is based on the X-ray diffractograms in Figure 4.9, where it can be seen that the green tape has no secondary phases at all. Why the secondary phase forms, however, is not clear. Wang et al.[24] reported that a secondary phase of tetragonal tungsten bronze structure formed via abnormal grain growth from the fine-grained matrix of a KNNLT composition similar to the one in this study, containing 4 mol% Li, 20 mol% Ta and having a K/Na ratio of 50/50. They explained this phenomenon by volatilization of potassium from the material at high temperatures, which breaks the stoichiometry and triggers the formation of a sodium-deficient secondary phase. The remaining sodium, which is less volatile than potassium, then migrates from the secondary phase to the matrix, with the diffusion of sodium determining the growth of the secondary phase.

It is not known what triggers the formation of the secondary phase in the textured KNNLT-Mn(A) material. From the BSE image of the material (Figure 4.7(d)) the secondary phase seems to form large, elongated grains that are oriented in the tape casting direction, i.e., it is textured. This suggests that the KNN template particles play an important role in the formation of the secondary phase. It should be kept in mind that the templates are made from pure KNN, which gives rise to a small compositional deviation between templates and matrix in t-KNNLT-Mn(A). In KNN, the percentage of sodium on A-sites

is 50 %, while in KNNLT-Mn(A) it is 52 %. If the sodium content is important for formation and growth of secondary phases, as suggested by Wang et al.,[24] this initial difference might act as a trigger for further phase separation, possibly enhanced by evaporation of potassium at the high temperatures used for sintering (1150 °C for KNNLT-Mn(A)).

Optimal texturing of KNN-based materials

The textured materials that have been investigated here, can be described as having a $(0kl)$ texture, as the needle-shaped KNN templates are oriented such that the [100] direction (referred to the pseudo-cubic unit cell) is parallel to the tape casting direction. If the template particles rotate freely, as depicted in Figure 2.10(b), the possible polarization directions will lie on two cones and a disc as shown. The optimal orientation of a rotator ferroelectric crystal is such that the polar directions form a certain angle with the direction of poling or piezoelectric measurement, with the optimal angle governed by Equation (2.5). This is more likely to happen for a (001)-textured material, as in Figure 2.11(a), than in a $(0kl)$-textured material (or, similarly, a $(hk0)$-textured material, as in Figure 2.11(b)).

The best possibility for taking benefit of the templates used in this work, is if they can be made *not* to rotate freely as in Figure 2.10(b), but instead to lie "flat" as in Figure 2.10(a), with one of the pseudo-cubic directions [010] or [001] normal to the surface. In this way, the material could be described as having (010) and (001) texture, instead of the $(0kl)$ texture that develops upon free rotation of the templates. The question is then whether it would in fact be possible to rotationally orient the particles in this manner. According to Jones et al.,[28] this has been achieved with [001]-grown needle-shaped particles of lead metaniobate, $PbNb_2O_6$, that were used as templates for tape casting in the same way as in this work. Neutron diffraction was used to confirm that [100] and [010] preferred orientations developed in the normal and transverse directions (and, as expected, an [001] preferred orientation developed in the tape casting direction). It was also found that the rotational orientation, leading to [100] and [010] preferred orientations in the normal and transverse directions, depended on both the amount of template particles, the casting speed and the viscosity of the slurry used for tape casting. Higher casting speed or viscosity both increase the shear forces acting on the slurry, in turn increasing the rotational orientation of the templates. Both an increase in casting speed and in slurry viscosity will therefore be beneficial for the texturing procedure used here, in

that it is likely to increase the number of template particles that are (010)- or (001)-oriented, as compared to those that are $(0kl)$-oriented.

Another possibility for achieving beneficial texture in rotator ferroelectric materials, which is arguably easier, is to produce (001)-oriented materials. This is, as mentioned before, the procedure that was used by Saito et al.,[5] and was illustrated in Figure 2.11(a). Following the work of Madaro et al.,[27,41] one possible type of (001)-oriented templates could be KNN platelets made by molten salt conversion of $K_4Nb_6O_{17}$ or, possibly, KNb_3O_8. Using these particles as templates, it should be possible to introduce a beneficial (001) texture in the ceramics by normal tape casting. The challenge of needle-shaped [100]-grown particles needing to be rotationally oriented during tape casting, would not be an issue with this method.

Texture of t-KNNLT-Mn(A)

The Lotgering factors indicate the possibility of a high degree of orientation in the dense t-KNNLT-Mn(A), based on the relatively high degree of orientation in the green tape ($f = 22$ %) and the increase in Lotgering factor in the KNN-Mn sample during sintering, from $f = 5$ % to $f = 21$ %. As the t-KNNLT-Mn(A) contains large amounts of a secondary phase, the degree of texture in the material is not what determines the piezoelectric properties. Still, knowledge of the texture is interesting from a material processing standpoint, and as a tool for judging the suitability of the texturing method used here, even if it is not the optimal method for this particular material.

As the X-ray diffraction lines from the perovskite phase in t-KNNLT-Mn(A) all overlap to some degree with diffraction lines from the secondary phase (Figure 4.9), it is hard to judge the degree of texture from the X-ray diffractograms. It can be seen that the diffraction lines from the secondary phase at 2θ-values of approximately 25° and 29° have different intensity ratios in the experimental pattern as opposed to the pattern reported for $K_3Li_2Nb_5O_{15}$, but as this is probably not the exact composition of the secondary phase in t-KNNLT-Mn(A), this observation can hardly be used to extract quantitative information about the material.

A different method for obtaining information about texture in crystalline materials, is orientation imaging microscopy by electron backscatter diffraction (EBSD). This method has previously been used by the author to determine the degree of orientation in textured KNN-based materials.[6] The main strength of the method is that it can distinguish between phases with different crystal structures, making it possible to separate the orthorhombic perovskite phase

from the secondary phase of tetragonal symmetry. Each phase can then be analyzed with respect to crystal orientation, to see if one or both of the phases has a certain texture. A further advantage of the technique is that it actually images the grains in the sample surface, making it possible to see grains and grain boundaries that are hard to observe by other microscopy techniques. Micrographs obtained by EBSD can thus be used as a complement to regular SEM micrographs like those shown in Figure 4.7, to give detailed information about the microstructure of the material.

A weakness of the EBSD technique, on the other hand, is the difficulty in preparation of samples, especially for non-conducting ceramics. Extreme care must be taken during grinding and polishing of the sample in order to obtain a smooth surface, free of defects like grain pullouts. Charging of samples is also an issue for non-conducting materials when observed in the scanning electron microscope, and while low vacuum or careful coating of the sample are possible ways of dealing with this problem, both degrade the quality of the information obtained by EBSD. Finally, the crystal structure of the phases that are to be investigated, must be known in order to obtain useful information from the scans. The phases must also be sufficiently different with respect to symmetry and unit cell parameters, in order to be distinguished by this technique. Still, if carefully done, EBSD could provide useful information about KNN-based materials that can not be obtained by other means.

Chapter 6

Concluding remarks and further work

A procedure for the synthesis of textured KNN-based lead-free piezoelectric materials has been investigated, both with regards to the texturing procedure itself, and suitable materials in the KNN family (KNN/KNNLT).

The texturing procedure, using [100]-grown needle-shaped template particles of KNN to obtain $(0kl)$-textured samples, is probably not optimal for KNN and KNNLT doped with Mn. The piezoelectric anisotropy of the materials is such that a (001) texture is more beneficial, which would be easier to achieve using (001)-oriented platelets instead of needles as templates for texturing. This should be explored in the case of further work on texturing of KNN-based materials.

Regarding materials, both KNN and KNNLT compositions have been investigated as candidates for production of textured piezoelectric ceramics with respect to sintering behaviour and piezoelectric properties. KNN with addition of manganese (KNN-Mn) and KNNLT with manganese substituted to the A site of the perovskite lattice (KNNLT-Mn(A)) have both been used for synthesis of textured and non-textured materials. KNNLT-Mn(A) sinters to the highest densities, reaching 96.7 % and 91.2 % of theoretical density for the non-textured and textured materials, respectively, while corresponding numbers for KNN-Mn are 93.9 % and 89.2 %.

The piezoelectric coefficient is higher for the non-textured samples of KNNLT-Mn(A) than for KNN-Mn, but the textured KNNLT-Mn(A) does not perform better than the textured KNN-Mn materials. This is due to the forma-

tion of a secondary phase in the KNNLT-Mn(A) material when it is textured. It is suggested that the use of KNN templates for texturing of KNNLT-Mn(A) triggers the formation of this phase by introducing a small stoichiometric inhomogeneity.

Appendix A

Crystallographic considerations

A.1 Evolution of polar directions in KNN

Upon cooling, a KNN crystal undergoes several phase transitions. The high-temperature form belongs to the cubic class $m\bar{3}m$, which is centrosymmetric and thus non-piezoelectric. The unit cell is therefore a cube, with no distinction between the three crystallographic axes. The cubic unit cell is shown in Figure A.1(a), with the central niobium atom and the oxygen octahedron indicated.

When cooled to approximately 400 °C, the first phase change occurs. The crystal is transformed into the tetragonal class $4mm$, which is piezoelectric. With respect to the cubic unit cell defined earlier, this phase change leads to one of the three axes of the unit cell being elongated, along with a displacement of the central niobium atom in the same direction. This axis, which is now distinguishable from the other two, is conventionally called the z axis, and becomes the polar axis of the tetragonal unit cell, as illustrated in Figure A.1(b). Since the elongation of the unit cell can occur along any of the three crystallographic axes of the cubic cell, there are six possible directions of spontaneous polarization (the $\langle 100 \rangle$ set of directions) in the tetragonal phase, directed towards the middle of the six faces of the unit cell.

Continuing the cooling, a new phase transition occurs at approximately 200 °C. The tetragonal phase is then transformed to an orthorhombic phase of class $mm2$. With respect to the original cubic unit cell, all three axes are now distinguishable, with different lengths. The two axes that were indistinguishable in the tetragonal phase are now termed the x and y axes (depending on

how these are chosen, the crystal class is referred to as *Amm*2 or *Bmm*2, the differences between which will be discussed later). The central niobium atom is displaced further, now along one of the x and y axes in addition to along the z axis. The polar direction is therefore now towards the middle of a unit cell edge, of which there are twelve in total. There are therefore twelve possible polarization directions in the orthorhombic phase (the $\langle 110 \rangle$ set of directions), of which one is shown in Figure A.1(c).

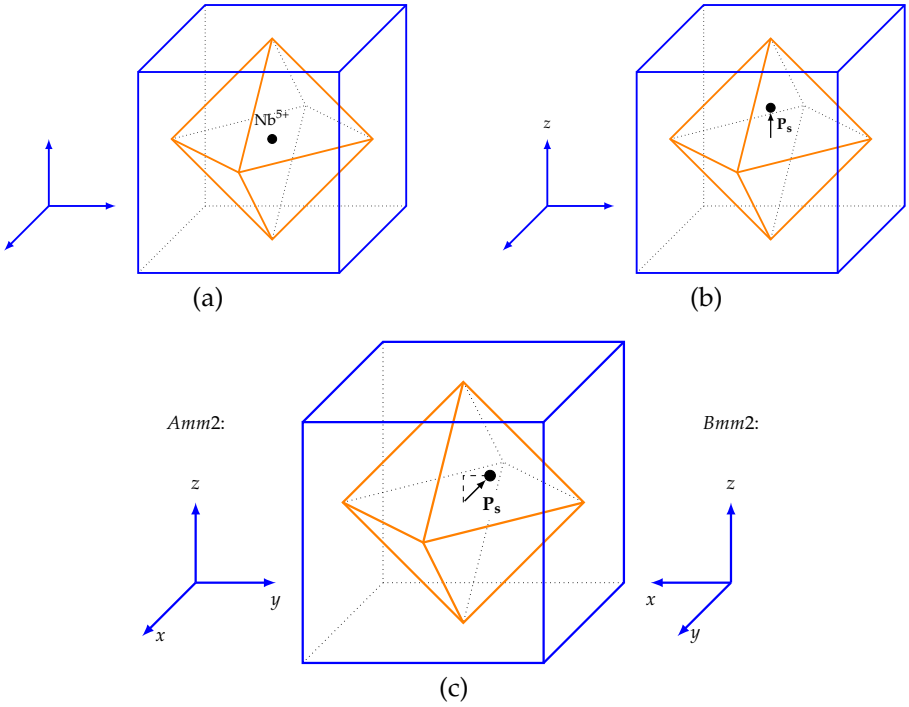

FIGURE A.1: Illustration of how the direction of spontaneous polarization in KNN (vector $\mathbf{P_s}$) changes with respect to the pseudo-cubic unit cell upon cooling through the (a) cubic, (b) tetragonal and (c) orthorhombic phases. Alkali ions are situated at the corners of the cubic cell, oxygen ions at the apices of the octahedron.

A.2 Pseudo-cubic and orthorhombic coordinates

So far, the discussion of crystallographic directions in KNN crystals has been with respect to the cubic unit cell of the high-temperature phase. It is a common practice to give coordinates that refer to this cell, even when discussing phases that are not actually cubic. However, for the orthorhombic phase, another unit cell is sometimes chosen, namely the orthorhombic unit cell. This is a unit cell chosen so that it represents the orthorhombic symmetry of the phase more closely than does a pseudo-cubic unit cell. A sketch of the orthorhombic unit cell is shown in Figure A.2, and should be compared with Figure A.1(c). To clarify which unit cell a given set of coordinates refers to, subscripts are often used. For pseudo-cubic coordinates, one may write $[uvw]_{\mathrm{pc}}$, and for orthorhombic coordinates $[uvw]_{\mathrm{o}}$.

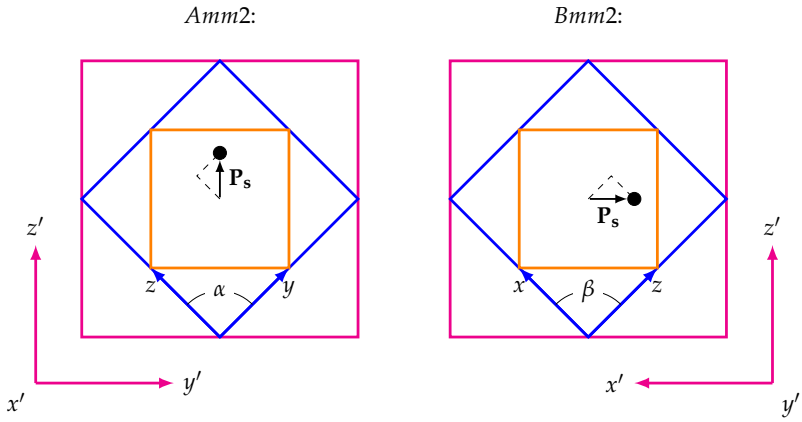

FIGURE A.2: Projections of orthorhombic unit cells for KNN. The *Amm*2 cell (left) is projected along the x' axis, the *Bmm*2 cell (right) along the y' axis.

In the pseudo-cubic unit cell, all three sides of the unit cell are approximately 4 Å, while in the orthorhombic unit cell, two of the sides are longer by a factor of approximately $\sqrt{2}$. Which of the sides are longer, depends on whether the *Amm*2 or *Bmm*2 convention is used, as shown in Figure A.2. In the *Amm*2 cell, the x' axis is the shorter one, while in the *Bmm*2 cell, it is the y' axis. Figure A.2 also makes it possible to deduce the following formulae for converting between the pseudo-cubic (a, b, c) and orthorhombic (a', b', c') unit cell parameters (using

the *Amm*2 convention):

$$
\begin{aligned}
a' &= a \\
b' &= b \sin\left(\frac{\alpha}{2}\right) + c \sin\left(\frac{\alpha}{2}\right) \\
c' &= c \cos\left(\frac{\alpha}{2}\right) + b \cos\left(\frac{\alpha}{2}\right)
\end{aligned}
$$

When using the *Bmm*2 convention, a and b are swapped, and α is replaced by β.

The differences between pseudo-cubic and orthorhombic coordinates are summed up in Table A.1. The table also gives vector coordinates for the crystallographic directions with a positive component along the pseudo-cubic z axis (the $[001]_{\mathrm{pc}}$ direction). These are the favourable polarization directions when the crystal is poled with an electric field in the $[001]_{\mathrm{pc}}$ direction.

TABLE A.1: Comparison of the pseudo-cubic (pc) and orthorhombic (o) representations of the KNN structure using the *Amm*2 and *Bmm*2 conventions. Angles are 90° unless otherwise specified.

*Amm*2		*Bmm*2	
pc	o	pc	o
Unit cell parameters:			
$a \approx 4$ Å	$a' \approx 4$ Å	$a \approx 4$ Å	$a' \approx 4\sqrt{2}$ Å
$b \approx 4$ Å	$b' \approx 4\sqrt{2}$ Å	$b \approx 4$ Å	$b' \approx 4$ Å
$c \approx 4$ Å	$c' \approx 4\sqrt{2}$ Å	$c \approx 4$ Å	$c' \approx 4\sqrt{2}$ Å
$\alpha \approx 90°$		$\beta \approx 90°$	
Selected crystallographic directions:			
$[011]$	$[001]$	$[\bar{1}01]$	$[\bar{1}00]$
$[101]$	$[2\bar{1}1]$	$[011]$	$[\bar{1}21]$
$[0\bar{1}1]$	$[0\bar{1}0]$	$[101]$	$[001]$
$[\bar{1}01]$	$[\bar{2}\bar{1}1]$	$[0\bar{1}1]$	$[\bar{1}\bar{2}1]$

Appendix B

The piezoelectric tensor

B.1 Tensor and matrix notation

Here, an overview is given of the mathematical description of piezoelectricity, more specifically the relation between the so-called tensor and matrix notations is given. The material is based mainly on chapters I, VII and IX of the book on crystal properties by J. F. Nye.[11]

As is the case with many properties of crystals, piezoelectricity is a highly anisotropic property. This makes a mathematical description of the phenomenon rather more complicated than for isotropic properties, such as for instance density. An electric polarization is generally described by a vector:

$$\mathbf{P} = \begin{pmatrix} P_1 \\ P_2 \\ P_3 \end{pmatrix},$$

and a state of stress in a material is properly described by a second-rank tensor (that is, a matrix):

$$\sigma_{jk} = \begin{pmatrix} \sigma_{11} & \sigma_{12} & \sigma_{13} \\ \sigma_{21} & \sigma_{22} & \sigma_{23} \\ \sigma_{31} & \sigma_{32} & \sigma_{33} \end{pmatrix}.$$

The relations describing the piezoelectric effect then become

$$P_i = d_{ijk}\sigma_{jk} \tag{B.1}$$

$$\epsilon_{jk} = d_{ijk}E_i, \tag{B.2}$$

with summation over repeated indexes implied, and i, j, k ranging over 1,2,3. P_i are the components of the polarization vector, σ_{jk} and ϵ_{jk} are the components of the stress and strain tensors, respectively, and E_i are the components of the electric field vector. The coefficients relating these quantitites form a third-rank tensor d_{ijk}, known as the *piezoelectric tensor*, and is the same in both equations.

Equation (B.1) states that all three components P_i of the polarization vector are linearly dependent on all the nine stress components σ_{jk}. For the component of **P** in the x direction, for example, Equation (B.1) gives

$$\begin{aligned} P_1 = \quad & d_{111}\sigma_{11} + d_{112}\sigma_{12} + d_{113}\sigma_{13} \\ & + d_{121}\sigma_{21} + d_{122}\sigma_{22} + d_{123}\sigma_{23} \\ & + d_{131}\sigma_{31} + d_{132}\sigma_{32} + d_{133}\sigma_{33}, \end{aligned} \tag{B.3}$$

and there are similar equations for P_2 and P_3. Similarly, Equation (B.2) states that each of the nine components ϵ_{jk} of the strain tensor depends linearly upon all three components E_i of the electric field vector.

A second-rank tensor, such as the stress tensor σ_{jk}, is a 3×3 matrix. A third-rank tensor, like d_{ijk}, can be thought of as a cube-shaped array made up of three layers, each consisting of a 3×3 matrix. The first subscript of d_{ijk} then refers to the layer, the second to the row, and the third to the column. Accordingly, there is a total of $3^3 = 27$ components of a third-rank tensor:

$$\begin{array}{ccc} i = 1: & i = 2: & i = 3: \\ \begin{pmatrix} d_{111} & d_{112} & d_{113} \\ (d_{121}) & d_{122} & d_{123} \\ (d_{131}) & (d_{132}) & d_{133} \end{pmatrix} & \begin{pmatrix} d_{211} & d_{212} & d_{213} \\ (d_{221}) & d_{222} & d_{223} \\ (d_{231}) & (d_{232}) & d_{233} \end{pmatrix} & \begin{pmatrix} d_{311} & d_{312} & d_{313} \\ (d_{321}) & d_{322} & d_{323} \\ (d_{331}) & (d_{332}) & d_{333} \end{pmatrix} \end{array}$$

Not all components of the piezoelectric tensor are independent of each other, however. The stress tensor σ_{ij} is symmetrical for a body in equilibrium (that is, $\sigma_{ij} = \sigma_{ji}$). Because of this, d_{ijk} must also be symmetrical in j and k (that is, $d_{ijk} = d_{ikj}$), meaning that there are only 18 independent components (redundant components are enclosed in parentheses in the array above). Taking into account the symmetry of σ_{ij} and d_{ijk}, the equations for piezoelectricity can be simplified by re-indexing the tensor components according to the following

scheme (showing only independent components):

$$\begin{pmatrix} d_{i11} & d_{i12} & d_{i13} \\ & d_{i22} & d_{i23} \\ & & d_{i33} \end{pmatrix} \rightarrow \begin{pmatrix} d_{i1} & \frac{1}{2}d_{i6} & \frac{1}{2}d_{i5} \\ & d_{i2} & \frac{1}{2}d_{i4} \\ & & d_{i3} \end{pmatrix}$$
$$\begin{pmatrix} \sigma_{11} & \sigma_{12} & \sigma_{13} \\ & \sigma_{22} & \sigma_{23} \\ & & \sigma_{33} \end{pmatrix} \rightarrow \begin{pmatrix} \sigma_1 & \sigma_6 & \sigma_5 \\ & \sigma_2 & \sigma_4 \\ & & \sigma_3 \end{pmatrix}$$

Using this new notation, the nine-term expression for P_1 in (B.3) is shortened down to six terms:

$$P_1 = d_{11}\sigma_1 + d_{12}\sigma_2 + d_{13}\sigma_3 + d_{14}\sigma_4 + d_{15}\sigma_5 + d_{16}\sigma_6, \tag{B.4}$$

and Equation (B.1) can be rewritten in the simpler form

$$P_i = d_{ij}\sigma_j \ (i = 1, 2, 3; j = 1, 2, \ldots, 6),$$

with summation over j implied. Equivalently, it can be written in an even more compact way as the matrix equation

$$\mathbf{P} = \mathbf{d}\boldsymbol{\sigma},$$

with

$$\mathbf{P} = \begin{pmatrix} P_1 \\ P_2 \\ P_3 \end{pmatrix}, \quad \mathbf{d} = \begin{pmatrix} d_{11} & d_{12} & d_{13} & d_{14} & d_{15} & d_{16} \\ d_{21} & d_{22} & d_{23} & d_{24} & d_{25} & d_{26} \\ d_{31} & d_{32} & d_{33} & d_{34} & d_{35} & d_{36} \end{pmatrix}, \boldsymbol{\sigma} = \begin{pmatrix} \sigma_1 \\ \sigma_2 \\ \sigma_3 \\ \sigma_4 \\ \sigma_5 \\ \sigma_6 \end{pmatrix}.$$

Similarly, Equation (B.2) for the converse piezoelectric effect can be rewritten

$$\epsilon_j = d_{ij}E_i \ (i = 1, 2, 3; j = 1, 2, \ldots, 6)$$

with summation over i implied, or as a matrix equation

$$\boldsymbol{\epsilon} = \mathbf{d}^{\mathsf{T}}\mathbf{E}.$$

B.2 The piezoelectric tensor in different point groups

The piezoelectric tensor in principle consists of 18 independent components. However, for most piezoelectric crystals, there are much fewer due to the symmetry of the crystal. This can be rationalized through Neumann's principle, which may be stated as follows:

The symmetry elements of any physical property of a crystal must include the symmetry elements of the point group of the crystal.[11]

This means that for a piezoelectric crystal of the orthorhombic class $mm2$, such as KNN at ambient temperature, the piezoelectric tensor must also include the symmetry elements that make up the $mm2$ point group. By operating with the symmetry elements of $mm2$ on d_{ijk} and noticing how the components transform (the procedure is detailed in the book by Nye[11]), it can be seen that 13 of the 18 tensor components must be zero for Neumann's principle to hold. The result is the following reduction of the piezoelectric matrix $\mathbf{d}$:

$$\begin{pmatrix} d_{11} & d_{12} & d_{13} & d_{14} & d_{15} & d_{16} \\ d_{21} & d_{22} & d_{23} & d_{24} & d_{25} & d_{26} \\ d_{31} & d_{32} & d_{33} & d_{34} & d_{35} & d_{36} \end{pmatrix} \xrightarrow{mm2} \begin{pmatrix} 0 & 0 & 0 & 0 & d_{15} & 0 \\ 0 & 0 & 0 & d_{24} & 0 & 0 \\ d_{31} & d_{32} & d_{33} & 0 & 0 & 0 \end{pmatrix}$$

Hence, for crystals of class $mm2$, only five independent coefficients are needed for a complete description of the piezoelectric effect. For crystals of higher symmetry, the number of independent coefficients is even lower. An example of this is the tetragonal point group $4mm$, which is the point group of KNN at approximately 200 °C to 400 °C. For piezoelectric crystals belonging to this class, there are only three independent coefficients of $\mathbf{d}$:

$$\begin{pmatrix} d_{11} & d_{12} & d_{13} & d_{14} & d_{15} & d_{16} \\ d_{21} & d_{22} & d_{23} & d_{24} & d_{25} & d_{26} \\ d_{31} & d_{32} & d_{33} & d_{34} & d_{35} & d_{36} \end{pmatrix} \xrightarrow{4mm} \begin{pmatrix} 0 & 0 & 0 & 0 & d_{15} & 0 \\ 0 & 0 & 0 & d_{15} & 0 & 0 \\ d_{31} & d_{31} & d_{33} & 0 & 0 & 0 \end{pmatrix}$$

If an inversion center is present in a point group, all piezoelectric coefficients immediately vanish. As a result, all centrosymmetric crystals are non-piezoelectric. The high-temperature polymorph of KNN belongs to the cubic class $m\bar{3}m$, which is centrosymmetric. As a result, KNN at high temperatures is paraelectric rather that piezoelectric.

Appendix C

Piezoelectric data

Detailed results from piezo- and dielectric characterization are collected in this appendix. All figures, one per sample, contain the following subfigures:

(a) Polarization loops at bipolar fields from 15 kV cm^{-1} to 40 kV cm^{-1},

(b) strain loops at bipolar fields from 15 kV cm^{-1} to 40 kV cm^{-1},

(c) current loops at bipolar fields from 15 kV cm^{-1} to 40 kV cm^{-1}, and

(d) strain loops at unipolar fields from 15 kV cm^{-1} to 40 kV cm^{-1}.

Each type of subfigure is drawn to the same scale in all figure, so that for example bipolar strain loops can be directly compared between samples. Colours used in this appendix have no meaning other than to make it easier to distinguish between curves in the same plot.

All measurements were done at a frequency of 0.25 Hz.

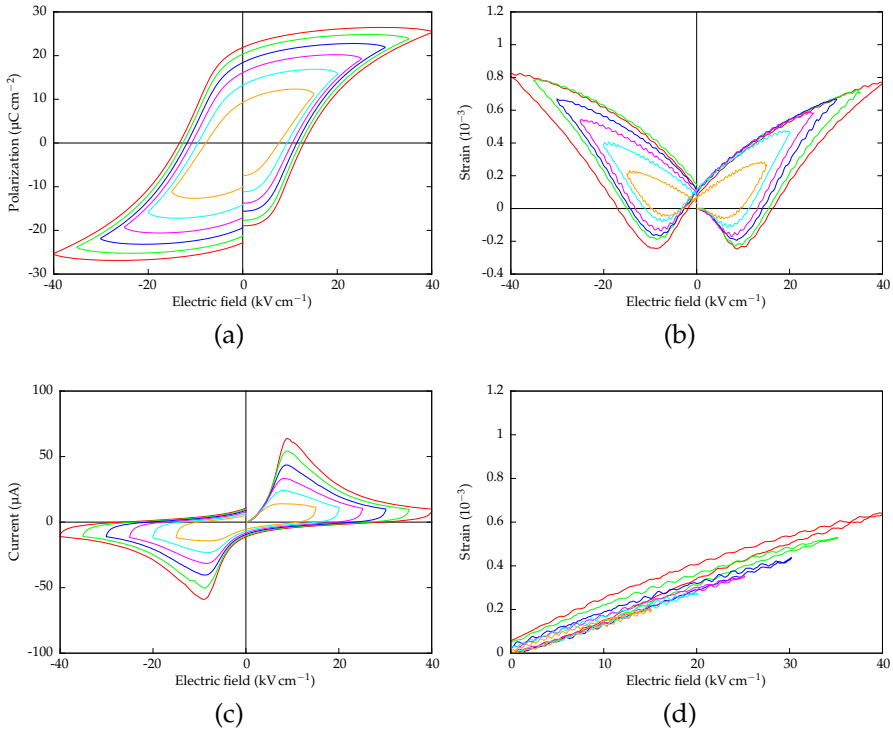

FIGURE C.1: KNN-Mn (3 h).

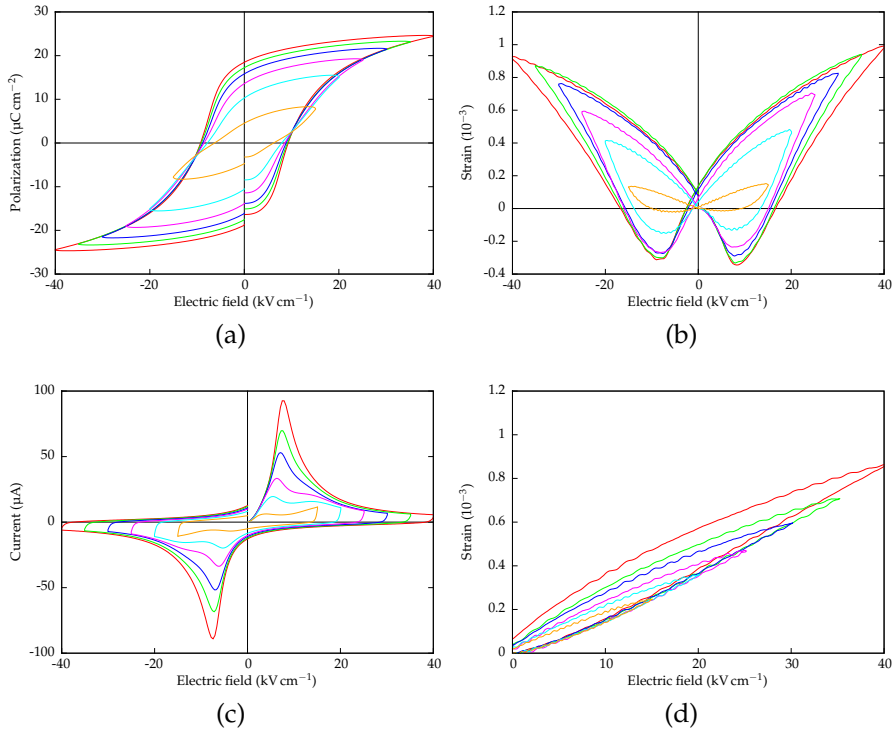

FIGURE C.2: KNN-Mn (14 h).

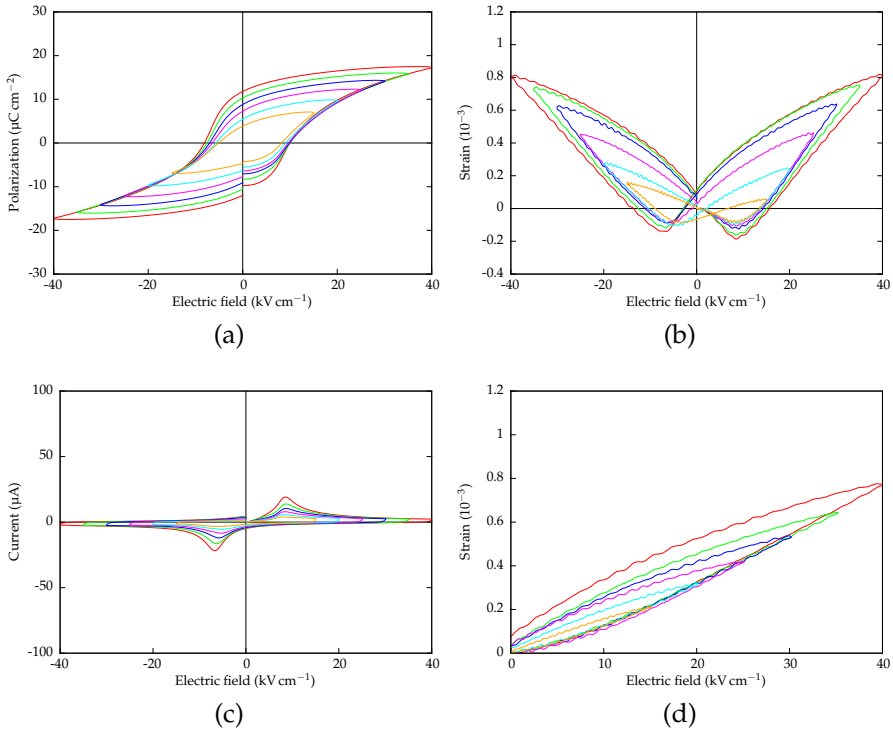

FIGURE C.3: t-KNN-Mn (14 h).

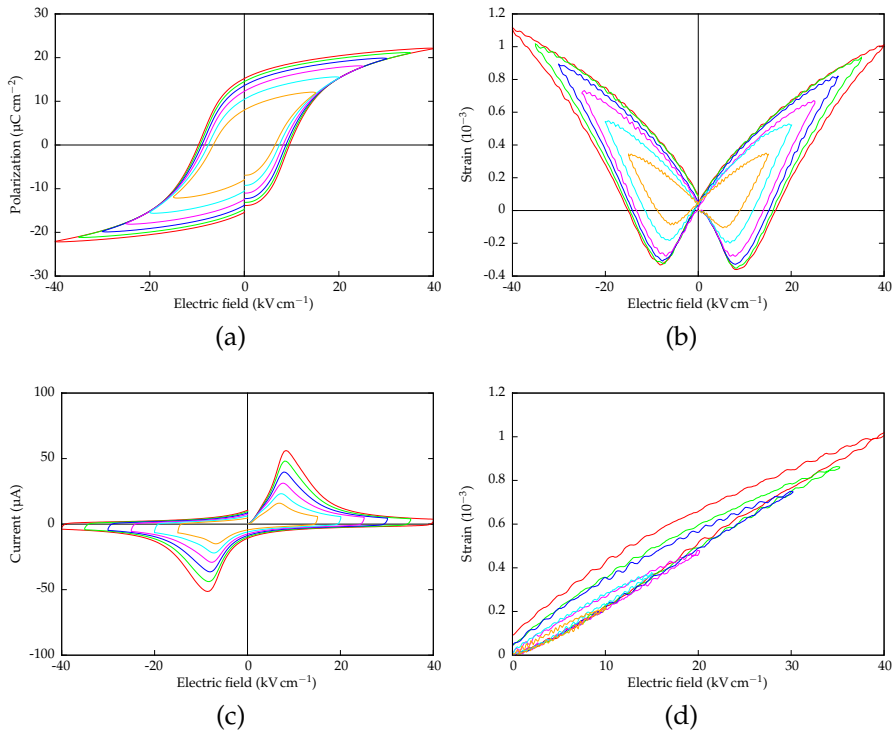

FIGURE C.4: KNNLT-Mn(A) (3 h).

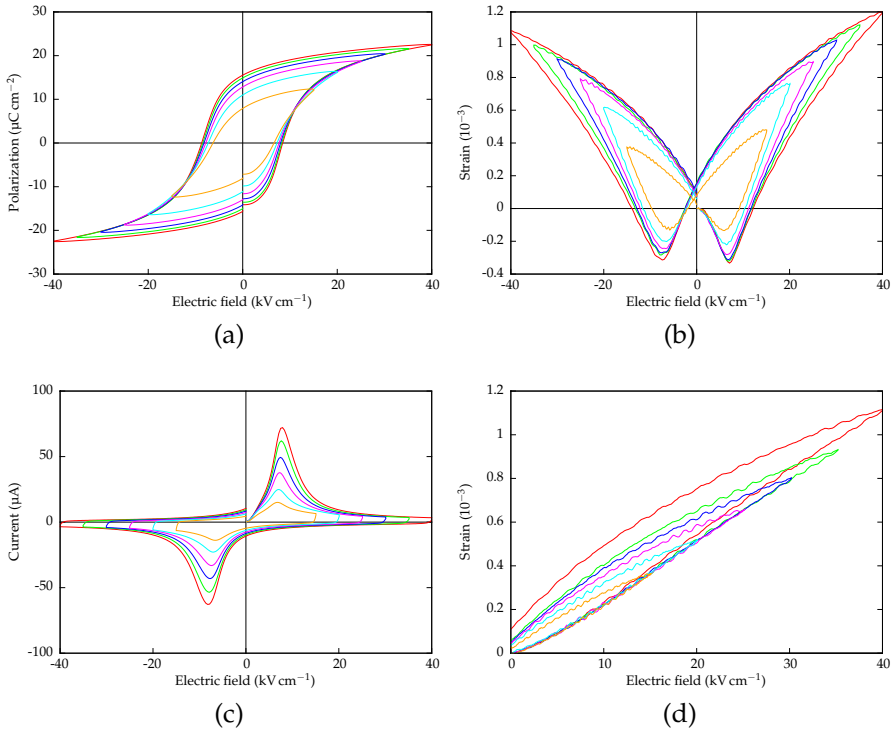

FIGURE C.5: KNNLT-Mn(A) (14 h).

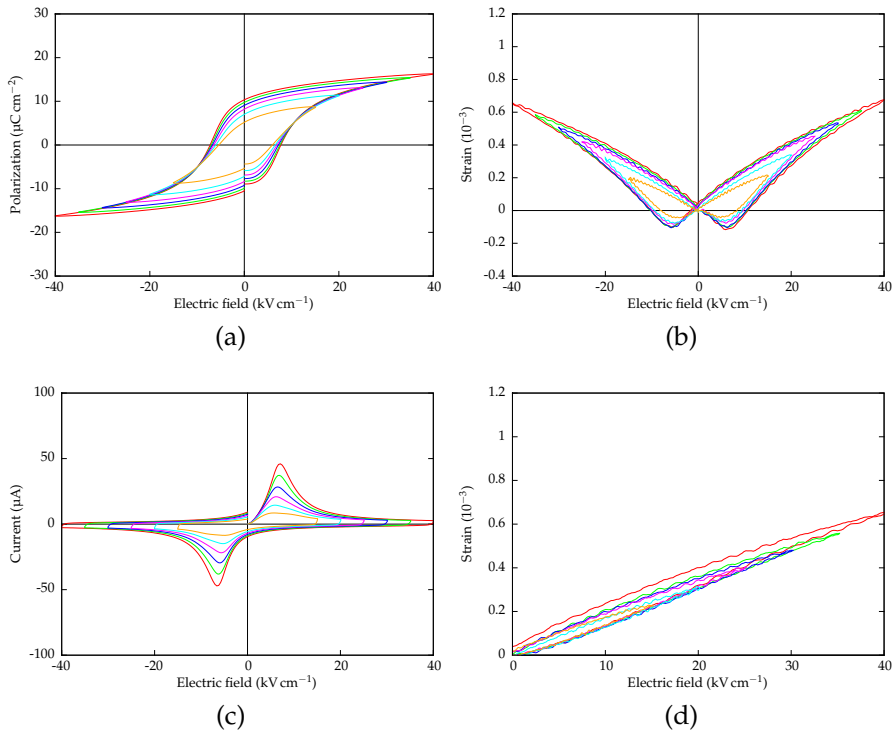

FIGURE C.6: t-KNNLT-Mn(A) (14 h).

Bibliography

[1] D. W. Richerson. *Modern Ceramic Engineering*. CRC Press, 2005.

[2] B. Jaffe, W. R. Cook, and H. Jaffe. *Piezoelectric Ceramics*. Academic Press Inc. (London) Ltd., 1971.

[3] *Directive 2002/95/EC of the European Parliament and of the Council on the restriction of the use of certain hazardous substances in electrical and electronic equipment*. Official Journal of the European Union. Jan. 2003.

[4] J. Rödel et al. "Perspective on the Development of Lead-free Piezoceramics". In: *Journal of the American Ceramic Society* 92.6 (June 2009), pp. 1153–1177. ISSN: 00027820. DOI: 10.1111/j.1551-2916.2009.03061.x.

[5] Y. Saito et al. "Lead-free piezoceramics". In: *Nature* 432.7013 (2004), pp. 84–87. DOI: 10.1038/nature03008.1..

[6] G. Olsen. "Texturing of lead-free piezoceramics". Specialization project. Norwegian University of Science and Technology, Dec. 2011.

[7] L.-P. Bjørkeng. "Sintring av $K_{0.5}Na_{0.5}NbO_3$keramer". In Norwegian. MSc thesis. Norwegian University of Science and Technology, July 2010.

[8] J. M. Strand. "Development of lead-free electroceramics – $K_{0.5}Na_{0.5}NbO_3$ substituted with Li & Ta". MSc thesis. Norwegian University of Science and Technology, June 2011.

[9] F. Madaro. "Synthesis of textured $K_xNa_{1-x}NbO_3$ materials". PhD thesis. Norwegian University of Science and Technology, Mar. 2010.

[10] A. J. Moulson and J. M. Herbert. *Electroceramics*. Second Edition. Wiley, 2003.

[11] J. F. Nye. *Physical properties of crystals*. Oxford University Press, 1985.

[12] A. L. Kholkin, N. A. Pertsev, and A. V. Goltsev. "Piezoelectricity and Crystal Symmetry". In: *Piezoelectric and Acoustic Materials for Transducer Applications*. Ed. by A. Safari and E. K. Akdoğan. Springer, 2008.

[13] L. Egerton and D. M. Dillon. "Piezoelectric and Dielectric Properties of Ceramics in the System Potassium–Sodium Niobate". In: *Journal of the American Ceramic Society* 42.9 (1959), pp. 438–442.

[14] D. W. Baker et al. "A comprehensive study of the phase diagram of $K_xNa_{1-x}NbO_3$". In: *Applied Physics Letters* 95.9 (2009), p. 091903. ISSN: 00036951. DOI: 10.1063/1.3212861.

[15] E. Hollenstein et al. "Piezoelectric properties of Li- and Ta-modified $K_{0.5}Na_{0.5}NbO_3$ ceramics". In: *Applied Physics Letters* 87.18 (2005), p. 182905. ISSN: 00036951. DOI: 10.1063/1.2123387.

[16] Y. Dai, X. Zhang, and G. Zhou. "Phase transitional behavior in $K_{0.5}Na_{0.5}NbO_3$-$LiTaO_3$ ceramics". In: *Applied Physics Letters* 90.262903 (2007). DOI: 10.1063/1.2751607.

[17] M. Matsubara et al. "Sinterability and Piezoelectric Properties of (K,Na)-NbO_3 Ceramics with Novel Sintering Aid". In: *Japanese Journal of Applied Physics* 43.10 (Oct. 2004), pp. 7159–7163. ISSN: 0021-4922. DOI: 10.1143/JJAP.43.7159.

[18] H.-Y. Park et al. "Effect of CuO on the Sintering Temperature and Piezoelectric Properties of $(Na_{0.5}K_{0.5})NbO_3$ Lead-Free Piezoelectric Ceramics". In: *Journal of the American Ceramic Society* 91.7 (July 2008), pp. 2374–2377. ISSN: 00027820. DOI: 10.1111/j.1551-2916.2008.02408.x.

[19] R. Zuo et al. "Sintering and Electrical Properties of Lead-Free $Na_{0.5}K_{0.5}NbO_3$ Piezoelectric Ceramics". In: *Journal of the American Ceramic Society* 89.6 (June 2006), pp. 2010–2015. ISSN: 0002-7820. DOI: 10.1111/j.1551-2916.2006.00991.x.

[20] L. Wang et al. "Enhanced ferroelectric properties in Mn-doped $K_{0.5}Na_{0.5}$-NbO_3 thin films derived from chemical solution deposition". In: *Applied Physics Letters* 97.7 (2010), p. 072902. ISSN: 00036951. DOI: 10.1063/1.3479530.

[21] S. Zhang et al. "Sintering Effect on Microstructure and Properties of $(K,Na)NbO_3$ Ceramics". In: *Journal of the American Ceramic Society* 94.11 (Nov. 2011). Ed. by A. Fetiera, pp. 3659–3665. ISSN: 00027820. DOI: 10.1111/j.1551-2916.2011.04833.x.

[22] Y. Zhen and J.-F. Li. "Normal Sintering of (K,Na)NbO_3-Based Ceramics: Influence of Sintering Temperature on Densification, Microstructure, and Electrical Properties". In: *Journal of the American Ceramic Society* 89.12 (Dec. 2006), pp. 3669–3675. ISSN: 0002-7820. DOI: 10.1111/j.1551-2916.2006.01313.x.

[23] J Li et al. "Normal sintering of (K,Na)NbO_3-based lead-free piezoelectric ceramics". In: *Ceramics International* 34.4 (May 2008), pp. 783–786. ISSN: 02728842. DOI: 10.1016/j.ceramint.2007.09.025.

[24] Y. Wang et al. "High-Temperature Instability of Li- and Ta-Modified (K,Na)NbO_3 Piezoceramics". In: *Journal of the American Ceramic Society* 91.6 (2008), pp. 1962–1970. DOI: 10.1111/j.1551-2916.2008.02392.x.

[25] J. Fang et al. "Narrow sintering temperature window for (K,Na)NbO_3-based lead-free piezoceramics caused by compositional segregation". In: *Physica Status Solidi (a)* 208.4 (Apr. 2011), pp. 791–794. ISSN: 18626300. DOI: 10.1002/pssa.201026500.

[26] G. L. Messing et al. "Templated Grain Growth of Textured Piezoelectric Ceramics". In: *Critical Reviews in Solid State and Materials Sciences* 29.2 (Apr. 2004), pp. 45–96. ISSN: 1040-8436. DOI: 10.1080/10408430490490905.

[27] F. Madaro et al. "Synthesis of anisometric $KNbO_3$ and $K_{0.5}Na_{0.5}NbO_3$ single crystals by chemical conversion of non-perovskite templates". In: *CrystEngComm* 13.5 (2011), p. 1350. ISSN: 1466-8033. DOI: 10.1039/c0ce00414f.

[28] J. L. Jones, B. J. Iverson, and K. J. Bowman. "Texture and Anisotropy of Polycrystalline Piezoelectrics". In: *Journal of the American Ceramic Society* 90.8 (Aug. 2007), pp. 2297–2314. ISSN: 0002-7820. DOI: 10.1111/j.1551-2916.2007.01820.x.

[29] M. Zgonik et al. "Materials constants of $KNbO_3$ relevant for electro- and acousto-optics". In: *Journal of Applied Physics* 74.2 (1993), p. 1287. ISSN: 00218979. DOI: 10.1063/1.354934.

[30] L. Liang et al. "Piezoelectric anisotropy of a $KNbO_3$ single crystal". In: *Journal of Applied Physics* 108.9 (2010), p. 094111. ISSN: 00218979. DOI: 10.1063/1.3511336.

[31] H. Nagata et al. "Evaluation of Piezoelectric Properties for $KNbO_3$-Based Ceramics". In: *Ferroelectrics* 381.1 (June 2009), pp. 191–195. ISSN: 0015-0193. DOI: 10.1080/00150190902876769.

[32] R. E. Newnham. *Properties of Materials: Anisotropy, Symmetry, Structure*. Oxford University Press, 2004.

[33] E. Li et al. "Miniature Ultrasonic Motor Using Shear Mode of Potassium Sodium Niobate-Based Lead-Free Piezoelectric Ceramics". In: *Japanese Journal of Applied Physics* 48.9 (Sept. 2009), 09KD11. ISSN: 0021-4922. DOI: 10.1143/JJAP.48.09KD11.

[34] J. B. Lim et al. "Shear-Mode Piezoelectric Properties of Modified-(K,Na)-NbO_3 Ceramics for "Hard" Lead-Free Materials". In: *Journal of the American Ceramic Society* 93.9 (June 2010), pp. 2519–2521. ISSN: 00027820. DOI: 10.1111/j.1551-2916.2010.03870.x.

[35] *ISO 5017:1998, Dense shaped refractory products — Determination of bulk density, apparent porosity and true porosity*. International Standard.

[36] F. Lotgering. "Topotactical reactions with ferrimagnetic oxides having hexagonal crystal structures–i". In: *Journal of Inorganic and Nuclear Chemistry* 9.1956 (1959), pp. 249–254.

[37] A. R. West. *Basic Solid State Chemistry*. Second Edition. Wiley, 1999.

[38] Y. Kizaki, Y. Noguchi, and M. Miyayama. "Defect control for low leakage current in $K_{0.5}Na_{0.5}NbO_3$ single crystals". In: *Applied Physics Letters* 89.14 (2006), p. 142910. ISSN: 00036951. DOI: 10.1063/1.2357859.

[39] D. Lin et al. "Influence of MnO_2 Doping on the Dielectric and Piezoelectric Properties and the Domain Structure in $(K_{0.5}Na_{0.5})NbO_3$ Single Crystals". In: *Journal of the American Ceramic Society* 93.4 (Apr. 2010), pp. 941–944. ISSN: 00027820. DOI: 10.1111/j.1551-2916.2009.03501.x.

[40] M. I. Morozov, H. Kungl, and M. J. Hoffmann. "Effects of poling over the orthorhombic-tetragonal phase transition temperature in compositionally homogeneous (K,Na)NbO[sub 3]-based ceramics". In: *Applied Physics Letters* 98.13 (2011), p. 132908. ISSN: 00036951. DOI: 10.1063/1.3573790.

[41] F. Madaro et al. "Molten salt synthesis of $K_4Nb_6O_{17}$, $K_2Nb_4O_{11}$ and KNb_3O_8 crystals with needle- or plate-like morphology". In: *CrystEngComm* 13.5 (2011), p. 1304. ISSN: 1466-8033. DOI: 10.1039/c0ce00413h.